

A Nonlinear Control Allocation Strategy for Dual Half Bridge Power Converters

Ricardo de Castro*, Rui Esteves Araujo†, Jonathan Brembeck‡,

* Dep. of Mechanical Engineering, University of California, Merced, 5200 N. Lake Road, Merced, CA 95343

‡ Department of Vehicle System Dynamics and Control, German Aerospace Center (DLR), Wessling, D-82234, Germany

†INESC TEC and Faculty of Engineering, University of Porto, Porto, 4200-465, Portugal

Abstract—This work focuses on designing nonlinear control algorithms for dual half-bridge converters (DHBs). We propose a two-layer controller to regulate the current and voltage of the DHB. The first layer utilizes a change in the control variable to obtain a quasi-linear representation of the DHB, allowing for the application of simple linear controllers to regulate current and power flow. The second layer employs a nonlinear control allocation algorithm to select control actions that fulfill (pseudo) power setpoints specified by the first control layer; it also minimizes peak-to-peak currents in the DHB and enforces voltage balance constraints. We apply the DHB and this new control strategy to manage power flow in a hybrid energy storage system comprising of a battery and supercapacitors. Numerical simulation results demonstrate that, in comparison with state-of-the-art approaches, our control algorithm is capable of maintaining good transient behavior over a wide operating range, while reducing peak-to-peak current by up to 80%.

Index Terms—power conversion, nonlinear control, dual half bridge converters, hybrid energy storage

Note to Practitioners—Dual half bridges (DHB) are an important class of converters that is used in a wide range of practical applications, including automotive and renewable energies. Despite their benefits—such as galvanic isolation, zero-voltage switching, and bidirectional power flow—the design of control algorithms for this converter is challenging due to its highly nonlinear response. In this work, we provide a new control framework that allows the designer to obtain a linear input-to-state representation of the converter and to “cancel” the dominant nonlinearities. The paper also presents the application of the parameter space tuning technique, which allows the designer to synthesize DHB controllers that fulfill transient, disturbance rejection, and robustness requirements. The tuning approach provides a set of possible controller gains that fulfill the control specifications (and not just a single value). This enables the application engineer to perform fine-tuning of the controller gains within a pre-certified parameter space that satisfies the control requirements, providing another important practical benefit.

I. INTRODUCTION

Batteries play a critical role in electrified transportation and renewable energy [1]. They enable zero local emissions in transportation [1] and allow storage of energy from intermittent sources like solar and wind, enhancing grid stability [2]. However, finding a single battery chemistry capable of fulfilling all the application requirements—such as low cost, high energy/power density and long duration—is difficult. To cope with this challenge, *hybrid energy storage systems (ESS)* can

be designed with multiple types of storage elements, such as batteries and supercapacitors (SCs), aiming to exploit the best features offered by each component [3], [4]. For example, SCs with high power density and durability are particularly suited to handle rapid power bursts, while battery packs with high energy density can provide the average power needs of the load. These characteristics have been leveraged to build *hybrid ESS* with battery and SCs in electric vehicles [5], rail systems [6] and grid-support systems [7].

Batteries and SCs can be hybridized passively (direct parallel connection) or semi-actively (via power converters). Passive hybridization is cost-effective since it lacks power electronics, but the power split is dictated by the storage elements’ internal impedance, limiting control over SC utilization [8], [9]. In contrast, semi-active *hybrid ESS* integrate SCs via power converters (see Fig. 1), enabling optimized power management to reduce energy losses, battery aging and peak loads [9], [10]. Various power converters can be used in semi-active *hybrid ESS*, from simple flyback converters to more complex Z-source, interleaved, and dual-bridge configurations [11]. This work focuses on dual half-bridge (DHB) converters (see Fig. 1). DHBs offer galvanic isolation, zero-voltage switching, and bidirectional power flow [12]. Their high-frequency transformer enables a wide voltage range, making them well-suited for SCs with highly variable state-of-charge [13]. Due to these advantages, DHBs are widely used in *hybrid ESS* [10], as well as in active battery balancing [14], battery chargers [15], and microgrids [16].

This work focuses on designing a control algorithm for DHBs in semi-active *hybrid ESS*. As shown in Fig. 1, the controller operates four switches— S_1 , S_2 (primary side) and S_3 , S_4 (secondary side)—with complementary switching to prevent short circuits, requiring only two unique PWM signals. Pulse-width modulation (PWM) strategies are typically applied to generate these signals. For example, single phase shift modulation [17] allows us to define the duration when the upper switch is “on” (referred to as duty cycle d), as well as the delay between the primary and secondary PWM phase carriers (known as phase shift ϕ) [18]. By manipulating these control signals (d, ϕ), the controller can achieve several objectives, including: (i) regulation of the current/power flow transferred between the primary and secondary sides of the DHB [19], (ii) minimizing ripple current in the DHB’s transformer and associated Ohmic losses [20], and (iii) controlling the voltage

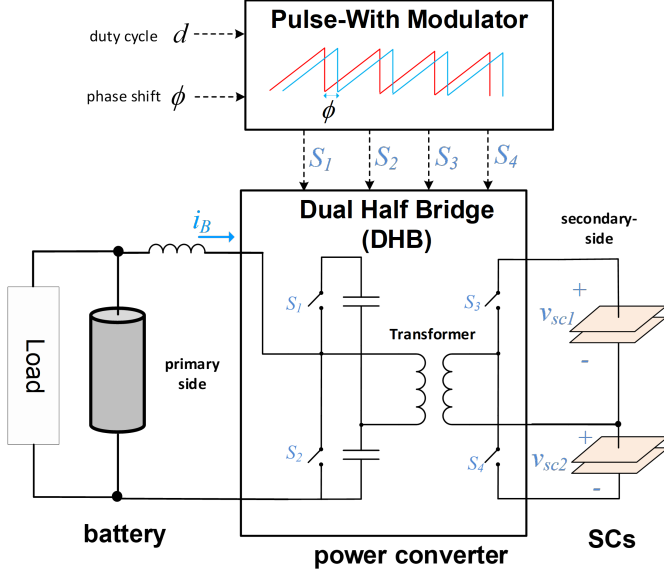


Fig. 1. Overview of the dual half bridge converter and its integration with a hybrid energy storage system composed of batteries and supercapacitors.

across different ports of the DHB [21].

Previous research on DHB control has primarily relied on linear model-based approaches. This typically begins with a reduced-order model, ranging from low-complexity average models that capture slow dynamics [18] to high-fidelity formulations, such as generalized average models [13] and discrete models [22], which better capture fast dynamics. Since these models are inherently nonlinear [13], [18], linearization techniques are commonly used to approximate converter behavior around an equilibrium point. However, these approximations are only valid for small-signal variations, limiting their effectiveness in dynamic conditions. Among linear control strategies, proportional-integral-derivative (PID) controllers are widely used due to their simplicity and ease of tuning [16], [18], [20], [23]. To enhance performance and robustness against parameter uncertainties, disturbance observers [24], sliding mode control [25], and adaptive control techniques [26] have also been explored for dual-bridge converters.

This work introduces a novel DHB control strategy that directly addresses the converter's nonlinearities. Instead of linearizing the converter around an equilibrium point, we propose a new change of control variable that transforms the original control inputs into a virtual control signal (w). This new control approach, inspired by input-to-output linearization techniques [27], provides three benefits. Firstly, it offers a linear representation of the DHB that remains valid for large signal variations, in contrast to the small-signal models discussed in prior literature [16], [18], [20], [23]. Secondly, the change of variable is robust against parametric uncertainties and relies solely on easily measurable voltage information. Thirdly, it enables the designer to construct the DHB controller in a linear space, leveraging a diverse range of synthesis control tools. To illustrate this advantage, we employ parameter space methods [28] to systematically synthesize a robust

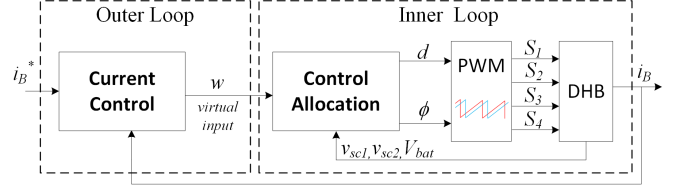


Fig. 2. Block diagram of the proposed control architecture: i) the *inner loop* maps the virtual input (w) to the duty cycle (d) and phase shift (ϕ); it utilizes control allocation techniques to minimize Ohmic losses and to cancel the nonlinear terms; ii) the *outer loop* regulates the current of the converter leveraging the linearized DHB model created by the inner loop.

linear controller capable of meeting various performance and robustness specifications for the DHB operation. It is worth noticing that input-output linearization techniques have been previously applied to numerous power converters, such as DFB [22], boost [29] and magnetically-coupled multiport dc-dc [30] converters. To the best of the authors' knowledge, our work provides the first application of input-output linearization to DHB converters.

The second contribution of this work focuses on the systematic exploitation of DHB's over-actuation. The DHB controlled with single phase-shift modulation [17] possesses two main degrees of freedom: duty cycle (d) and phase shift (ϕ). Different actuation combinations of (d, ϕ) can be employed to transfer the same power with the DHB. In this work, we leverage control allocation techniques [31] to select the best combination of control effort. As presented in Fig. 2, the control allocator splits the controller into two loops. The *outer loop* focuses on tracking DHB current using the linearized converter model enabled by the virtual control input w . The *inner loop* selects the final control input values in order to produce the requested virtual input, while handling actuation saturation and leveraging over-actuation to optimize secondary control goals, such as minimization of the Ohmic losses. Note that control allocation methods have been recently investigated in various application domains, such as automotive [32], aeronautics [33], [34], marine [35] and robotics [36]. To the best of the authors' knowledge, this is the first time that control allocation is applied to DHB converters.

The third contribution exploits the DHB's over-actuation to improve power conversion in *hybrid ESS*. To better understand this contribution, it is worth mentioning that the original DHB configuration proposed by [12], [18] was initially treated as a 2-port converter. In this work, we investigate the possibility of using the DHB in a 3-port configuration to regulate power flow in *hybrid ESS* composed of batteries and supercapacitors (SCs). As illustrated in Figure 1, our concept involves connecting the battery module to the primary side of the DHB, while the (two) secondary ports of the DHB are connected to two SC modules. This 3-port arrangement allows us to simultaneously regulate power flow between the two energy storage elements and balance the SCs' voltage. The SC balancing is important to prevent over-voltage conditions and to guarantee that the SC energy is fully used [37]. To achieve this goal, our work proposes a novel control allocation formulation that leverages the DHB's over-actuation to promote balancing of the SCs

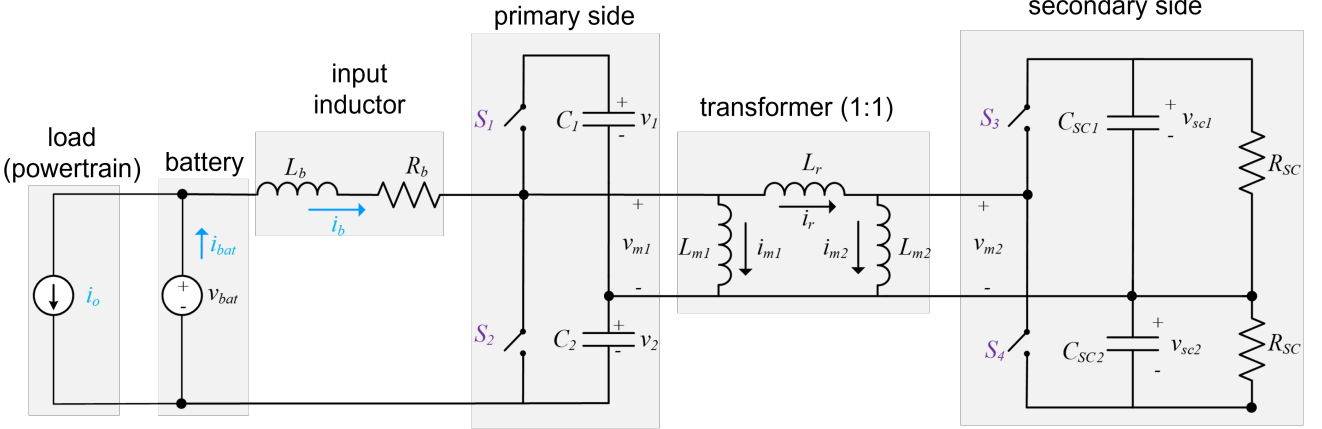


Fig. 3. Equivalent circuit of the dual half-bridge converter and its integration with the hybrid energy storage units (batteries and SCs).

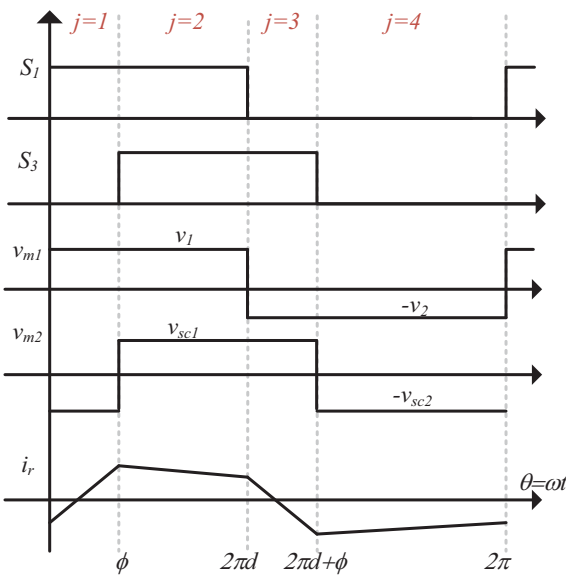


Fig. 4. Illustration of the four operating modes of the DHB converter and their effect in the voltage and current of the leakage inductor.

voltages.

A preliminary version of this work was presented at [38]. It is extended here with a new control allocation block and in-depth analysis of robustness and stability of the controller.

The remainder of this paper is structured as follows. Section II presents the mathematical model of the DHB converter, including its reduced-order formulation. Section III introduces the proposed control strategy, detailing the design of the *outer- and inner control loops*. Section IV provides an in-depth analysis of controller robustness, disturbance rejection, and stability. Section V presents simulation results that validate the effectiveness of the proposed approach. Finally, Section VI concludes the paper and outlines directions for future research.

II. CONVERTER MODEL

A. Overview

Fig. 3 shows the equivalent circuit of the DHB. It relies on the configuration proposed by [18] with one key modification: SCs are employed in the secondary side (C_{sc1}, C_{sc2}) instead of regular capacitors. This improves integration with the *hybrid ESS* and reduces component count. To model SC self-discharge, resistors (R_{sc}) are added in parallel. The converter's primary side connects to the battery (v_{bat}), an input inductor (L_b) with parasitic resistance (R_b), and two capacitors (C_1, C_2). A transformer, modeled using a π representation [39], links the primary and secondary sides, incorporating leakage inductance (L_r) and shunt magnetization branches (L_{m1}, L_{m2}). The powertrain load (e.g., motor inverter) is modeled as an ideal current source (i_o). To facilitate the control of the *hybrid ESS*, we employ the converter's input current (i_b) as one of the controlled variables. This enables us to regulate the power flow between the battery, load and the supercapacitors.

B. Slow Dynamics

The DHB converter is controlled by the on/off states of the primary (S_1, S_2) and secondary (S_3, S_4) switches. Since S_2 and S_4 operate complementary to S_1 and S_3 , the DHB has four operating modes $j \in \mathcal{J} = \{1, 2, 3, 4\}$, determined by switch positions (see Fig. 4). For each mode, the capacitor voltages ($v_1, v_2, v_{sc1}, v_{sc2}$) and inductor currents (i_b, i_r, i_{m1}, i_{m2}) evolve as follows:

$$\frac{dx}{dt} = A_{sx}^j x + A_{sr}^j i_r + A_{sm}^j i_m + B_s^j v_{bat} \quad (1a)$$

$$\frac{di_m}{dt} = A_{mx}^j x \quad (1b)$$

where $x = [i_b \ v_1 \ v_2 \ v_{sc1} \ v_{sc2}]^T$, i_r is the current in the leakage inductance and $i_m = [i_{m1} \ i_{m2}]^T$ the magnetization current vector. The battery voltage v_{bat} represents an exogenous input to the system. The constant matrices

TABLE I
MAPPING OF THE SWITCHING SIGNALS INTO THE DHB'S OPERATING MODES AND TRANSFORMER VOLTAGES (v_{m1}, v_{m2}).

Operating Mode	S_1	S_2	S_3	S_4	v_{m1}	v_{m2}
$j = 1$	1	0	0	1	v_1	$-v_{sc2}$
$j = 2$	1	0	1	0	v_1	v_{sc1}
$j = 3$	0	1	1	0	$-v_2$	v_{sc1}
$j = 4$	0	1	0	1	$-v_2$	$-v_{sc2}$

($A_{sx}^j, A_{sr}^j, A_{sm}^j, B_s^j, E_s^j, A_{mx}^j$) can be obtained via circuit analysis for each mode $j \in \mathcal{J}$ and are omitted here for the sake of brevity.

Pulse-width modulation is employed to generate the switching signals $S_n \in \{0, 1\}, n = 1, \dots, 4$. We consider a phase-shift carrier strategy, where a normalized triangular reference waveform $m(t) \in [0, 1]$ –also known as carrier waveform– is compared against a duty cycle $d \in [0, 1]$ to obtain the switching signals [17]. The primary switches signals are generated as:

$$S_1(d) = \text{sign}(d - m(t)) = \begin{cases} 1 & \text{if } d \geq m(t) \\ 0 & \text{otherwise} \end{cases} \quad (2)$$

with $S_2(d) = 1 - S_1(d)$ and $m(t)$ the carrier signal with switching frequency of ω_s . The secondary switches are commanded in a similar way, using the same duty cycle d , but reliant on a delayed carrier $m(t - \phi/\omega_s)$. The variable ϕ [rad] is called phase shift between the primary and secondary switching signals. The secondary switching signals are computed as

$$S_3(d, \phi) = \text{sign}(d - m(t - \phi/\omega_s)) \quad (3)$$

and $S_4(d, \phi) = 1 - S_3(d, \phi)$. The DHB operating mode is determined by mapping the switching signals S_n into \mathcal{J} , i.e., $j = \sigma(S_1(d, \phi), \dots, S_4(d, \phi)) : \{0, 1\}^4 \rightarrow \mathcal{J}$, where $\sigma(\cdot)$ is a function defined in Table I.

One challenge in (1) is related with the different time scales. Since the capacitors are designed with relatively high capacitance, low voltage ripple is usually obtained¹, yielding small variations in x during a switching period. On the other hand, the leakage inductance has a small value, and fast variations in the transformer current i_r are usually present during a switching period (see Fig. 4). As a result, (1a), (1b) represent the *slow dynamics* of the converter, while the dynamics of i_r (to be defined in the next section) captures the *fast dynamics*.

C. Fast Dynamics

Fig. 5 depicts the equivalent circuit of the *fast dynamics*, composed of the inductor L_r and two dependent voltage sources (v_{m1}, v_{m2}) that capture the voltage applied to the high-frequency transformer by the primary and secondary half bridges. Based on this equivalent circuit, the inductor current i_r can be modelled as

$$L_r \frac{di_r}{dt} = v_{m1}(j(t)) - v_{m2}(j(t)) \quad (4)$$

¹the same holds for the input inductor and current

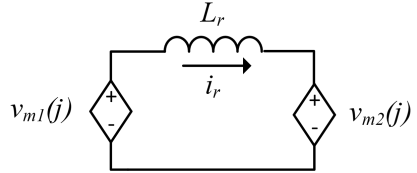


Fig. 5. Equivalent circuit for the *fast dynamics* of the DHB, which is captured by the current in the leakage inductance (i_r).

Note that voltages v_{m1}, v_{m2} vary with the operating mode of the converter j and are further dependent on the *slow dynamical* states x – see Table I and Fig. 4 for details. Assuming that x varies slowly over a switching period, the right side of the (4) becomes approximately constant. The leakage current can be computed via integration for each of the four operating modes of the converter. We apply the change of variable from time to angle ($\theta = \omega_s t$) to simplify the analytical analysis of i_r :

$$i_r(\theta, x, i_{r0}) = \begin{cases} (v_1 + v_{sc2}) \frac{\theta}{\omega_s L_r} + i_{r0} & 0 \leq \theta \leq \phi \\ (v_1 - v_{sc1}) \frac{\theta - \phi}{\omega_s L_r} + i_r(\phi, .) & \phi < \theta \leq 2\pi d \\ (-v_2 - v_{sc1}) \frac{\theta - 2\pi d}{\omega_s L_r} + i_r(2\pi d, .) & 2\pi d < \theta \leq 2\pi d + \phi \\ (-v_2 + v_{sc2}) \frac{\theta - 2\pi d - \phi}{\omega_s L_r} + i_r(2\pi d + \phi, .) & 2\pi d + \phi < \theta \leq 2\pi \end{cases}$$

where i_{r0} the transformer current at the beginning of the switching period, and $i_r(\theta, .) = i_r(\theta, x, i_{r0})$. Based on charge balance conditions for C_1, C_2 , the average value of i_r over one switching period is zero [19]

$$\int_0^{2\pi} i_r(\theta, x, i_{r0}) d\theta = 0 \quad (5)$$

This constraint can then be used to obtain the initial transformer current i_{r0} as function of x :

$$\begin{aligned} i_{r0}(x) = & (\pi d (d - 2) v_1 + \pi (d - 1)^2 v_2) / L_r \omega_s \quad (6) \\ & - d (\phi - 2\pi + \pi d) v_{sc1} / L_r \omega_s \\ & - (\pi - 2\pi d + d\phi + \pi d^2) v_{sc2} / L_r \omega_s \end{aligned}$$

D. Averaged Model

Combining the above results, the time-domain evolution of the leakage current can be expressed as $i_r^*(t, x) = i_r(\omega_s t, x, i_{r0}(x))$. Inserting this solution into (1a) allows us to represent the slow dynamics as:

$$\frac{dx}{dt} = A_{sx}^j x + A_{sr}^j i_r^*(t, x) + A_{sm}^j i_m + B_s^j v_{bat} \quad (7)$$

$$\frac{di_m}{dt} = A_{mx}^j x \quad (8)$$

for $j \in \mathcal{J}$. The dynamics of the average value of x and i_m (denoted X and I_m) can be obtained by averaging the right

hand side of the *slow dynamics* over one switching period [40]:

$$\begin{aligned}\frac{dX}{dt} &= \frac{1}{T_s} \sum_{j=1}^4 \int_{t_j}^{t_{j+1}} (A_{sx}^j X + A_{sr}^j i_r^*(t, X) \\ &\quad + A_{sm}^j I_m + B_s^j v_{bat}) dt \\ \frac{dI_m}{dt} &= \frac{1}{T_s} \sum_{j=1}^4 \int_{t_j}^{t_{j+1}} A_{mx}^j X dt\end{aligned}\quad (9)$$

where t_j and t_{j+1} correspond to the time instants when the converter switches between modes, which depend on the phase shift ϕ and duty cycle d (see Fig. 4); $T_s = 2\pi/\omega_s$ is the switching period. This is equivalent to:

$$\begin{aligned}\frac{dX}{dt} &= A_{sx}(u)X + A_{sm}(u)I_m + B_s V_{bat} \\ \frac{dI_m}{dt} &= A_{mx}(u)X\end{aligned}\quad (10)$$

where $u = [d \ \phi]^T$ is the control input, $X = [I_b \ V_1 \ V_2 \ V_{sc1} \ V_{sc2}]^T$ the average states, and $A_{sx}(u), A_{sm}(u), B_s, A_{mx}(u)$ matrices with polynomial dependence on u (see Appendix A for details). A word on the notation: in this section, average values of *slow* states are represented in upper case.

E. Reduced-order Model

The above averaged model is challenging. The control input u has a nonlinear effect in the converter dynamics and some states (e.g. I_m) are not directly measured. To derive a practical model for the DHB, a couple of practical assumptions will be adopted. First, we assume that the average magnetization currents I_m operate close to *quasi-static* conditions, *i.e.* $dI_m/dt \approx 0$. Inspecting the vector field (10) reveals that the time-derivative of I_m is divided by a large magnetization inductances (L_{m1}, L_{m2}), which makes this a very slowly dynamics. We also assume that both the magnetization and self-discharge currents of the SCs are relatively small and can be neglected for control purposes, thus $R_{sc} \rightarrow \infty, I_m \approx 0$. These approximations can be justified by the large impedance of the (shunt) magnetization branches of the transformer and the high self-discharge resistance of the SCs. Introducing these approximations into the average model yields a differential-algebraic system of equations:

$$\frac{dX}{dt} \approx A_{sx}(u)X + B_s(u)V_{bat} \quad (11)$$

$$0 \approx A_{mx}(u)X \quad (12)$$

To further simplify the model, we focus on the dynamic evolution of the summation of voltages in the primary capacitors (V_{12}) and in the SCs (V_{sc}):

$$V_1 + V_2 = V_{12}, \quad V_{sc1} + V_{sc2} = V_{sc} \quad (13)$$

Combining these equations with (12) and assuming symmetric capacitors in the primary ($C_b = C_1 = C_2$) and secondary

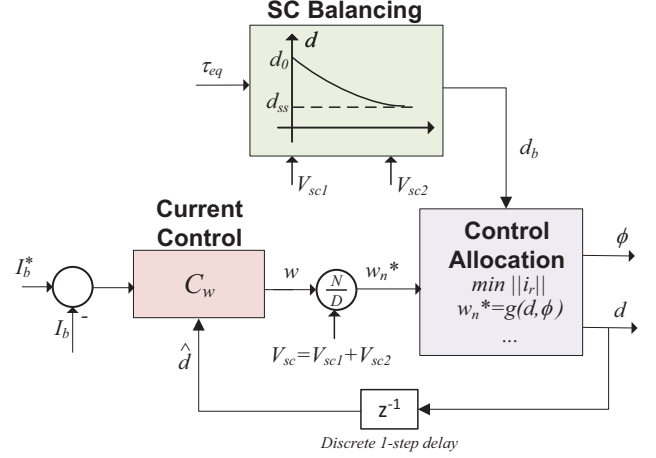


Fig. 6. Block diagram of the control algorithm.

($C_{sc} = C_{sc1} = C_{sc2}$) sides, allows us to obtain the following reduced-order model:

$$\frac{dI_b}{dt} = -\frac{R_b I_b}{L_b} - \frac{d}{L_b} V_{12} + \frac{1}{L_b} V_{bat} + \delta_1 \quad (14a)$$

$$\frac{dV_{12}}{dt} = \frac{2d}{C_b} I_b + \frac{\phi(4\pi d(d-1) + \phi)}{2C_b L_r \omega_s \pi} V_{sc} + \delta_2 \quad (14b)$$

$$\frac{dV_{sc}}{dt} = -\frac{\phi(4\pi d(d-1) + \phi)}{2C_{sc} L_r \omega_s \pi} V_{12} + \delta_3 \quad (14c)$$

$$\begin{bmatrix} V_1 \\ V_2 \\ V_{sc1} \\ V_{sc2} \end{bmatrix} = \begin{bmatrix} 0 & (1-d) & 0 \\ 0 & d & 0 \\ 0 & 0 & (1-d) \\ 0 & 0 & d \end{bmatrix} \begin{bmatrix} I_b \\ V_{12} \\ V_{sc} \end{bmatrix} \quad (14d)$$

where, $\delta_1, \delta_2, \delta_3$ are additive disturbance that capture parametric and non-parametric uncertainties that can be caused, for example, from the mathematical simplifications employed in this section. This reduced model contains 3 states (I_b, V_{12}, V_{sc}), 4 algebraic (voltage) constraints, 2 control inputs (d, ϕ) and 1 exogenous input (V_{bat}); it provides a compact, control-oriented representation of the DHB.

III. CONTROLLER DESIGN

This section introduces the algorithm for controlling the DHB. Our aim is to compute the duty cycle d and phase shift ϕ such that the following objectives are fulfilled:

- *Objective 1:* I_b should track a dynamic reference signal I_b^* while being robust against model uncertainties and disturbances (current control);
- *Objective 2:* minimize the magnitude of the transformer's current (i_r);
- *Objective 3:* balance the voltage in the two SCs modules, *i.e.*, $\Delta V_{sc} = V_{sc1} - V_{sc2} \approx 0$.

Objective 1 allow us to regulate the energy flow between the battery and SCs, while objective 2 contributes to the reduction of energy losses by minimizing the Ohmic losses. Objective 3 is important in order to make full use of the energy stored in the SCs; and also to avoid overvoltage conditions in the SCs, which might accelerate degradation and failure of the converter [37].

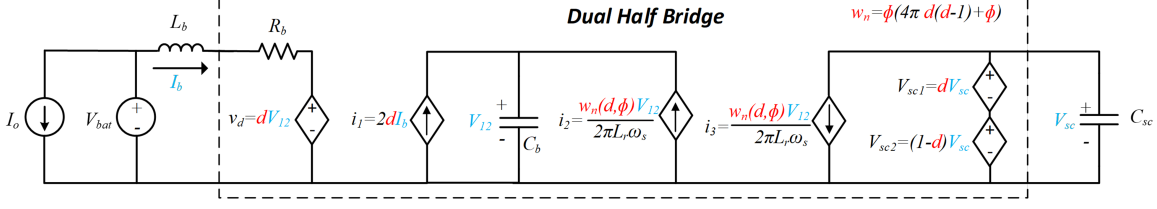


Fig. 7. Equivalent circuit of the reduced-order model of the DHB converter (*slow dynamics*). Variables in red (d, w_n) represent the control inputs, while variables highlighted in blue represent the main slow states (I_b, V_{12}, V_{sc}).

Fig. 6 provides an overview of the control architecture adopted in this work, which is composed of two control loops. The outer loop implements a current controller that manipulates a *virtual control input* w (to be defined shortly). The inner loop is a control allocator that maps w into the final control signal (d, ϕ) , while minimizing transformer current (i_r) and promoting voltage balancing in the SCs.

A. Outer Loop: Current Control

1) *Virtual Input:* The design of the current controller relies on input-output linearization [27]. It seeks to cancel the nonlinearities between the control inputs ($u = d, \phi$) and the output I_b . Inspecting (14), one can find that $\phi(4\pi d(d-1) + \phi)$ represents the main nonlinear term in the state-space model. This motivates us to define the following change of variable

$$w = \phi(4\pi d(d-1) + \phi) V_{sc} \quad (15)$$

where w is a *virtual control input*. Introducing w in (14) yields:

$$\frac{dI_b}{dt} = -\frac{R_b I_b}{L_b} - \frac{d}{L_b} V_{12} + \frac{1}{L_b} V_{bat} + \delta_1 \quad (16a)$$

$$\frac{dV_{12}}{dt} = \frac{2d}{C_b} I_b + \frac{1}{2C_b L_r \omega_s \pi} w + \delta_2 \quad (16b)$$

$$\frac{dV_{sc}}{dt} = -\frac{1}{2C_{sc} L_r \omega_s \pi} \frac{V_{12}}{V_{sc}} w + \delta_3 \quad (16c)$$

$$y_1 = I_b \quad (16d)$$

In this representation, the primary-side states (I_b, V_{12}) have linear dynamics (under the assumption of a slow-varying d), while the secondary-side state (V_{sc}) has a nonlinear behavior. To gain further insights into this model, Fig. 7 represents the equivalent circuit of (16). For ease of circuit analysis, we normalize the virtual control input relative to the SC voltage:

$$w_n = \frac{w}{V_{sc}} \quad (17)$$

The equivalent circuit is composed of three storage elements: the inductor L_b , the equivalent primary capacitor C_b and the secondary capacitor C_{sc} . These storage elements are connected to multiple dependent sources: i) voltage source v_1 captures the DHB voltage in the primary side; ii) the dependent current sources i_1, i_2, i_3 enables the exchange of power between the battery, C_b and C_{sc} and iii) voltage sources V_{sc1} and V_{sc2} model the voltages in the DHB's secondary sides. The equivalent circuit also allows us to better understand the role of the (normalized) virtual input in this exchange of power:

- when $w_n = 0$, the current source i_3 becomes an open circuit and no energy is exchanged with C_{sc} .
- when $w_n > 0$, the current source i_3 discharges C_{sc} . This energy is then transferred to i_2 , which can then directly charge C_b or the battery (via i_1).
- when $w_n < 0$, the current source i_2 discharges C_b and/or “pulls current” from the input inductor (via i_1). This discharge energy is then transferred to C_{sc} (via i_3).

It is also useful to analyze the steady-state power absorbed by the DHB. This can be expressed as²:

$$p_{in} = I_b v_d - R_b I_b^2 = I_b d V_{12} - R_b I_b^2 \quad (18)$$

$$= -\frac{w_n V_{sc}}{4dL_r \omega_s \pi} d V_{12} - R_b \left(w_n \frac{V_{sc}}{4dL_r \omega_s \pi} \right)^2 \quad (19)$$

$$\approx -w_n \frac{V_{sc} V_{bat}}{4dL_r \omega_s \pi} \quad (20)$$

where the last approximation neglects the Ohmic losses. This equation highlights the fact that the DHB power is directly proportional to the virtual control input w_n .

2) *Transfer Function:* Let us now derive the transfer functions that relate (w, V_{bat}) with the current I_b :

$$I_b(s) = \frac{\alpha_w(d) \omega_n^2(d)}{\omega_n(d)^2 + \frac{R_b}{L_b} s + s^2} w(s) + \frac{\frac{1}{L_b} s V_{bat}(s)}{\omega_n(d)^2 + \frac{R_b}{L_b} s + s^2} + \sum_{i=1}^3 G_\delta \delta_i(s) \quad (21)$$

where $\omega_n^2(d) = 2d^2/(L_b C_b)$ is the natural frequency and $\alpha_w(d) = (4L_r \omega_s \pi d)^{-1}$ the steady-state gain between the control input w and the current I_b . The transfer function G_δ captures the impact of the disturbances δ_i into the response of the current I_b . The above expression can be further re-arranged as:

$$I_b(s) = G_w(s) w(s) + G_v(s) V_{bat}(s) + \underbrace{\sum_{i=1}^3 G_\delta \delta_i(s)}_{\sigma(s)} \quad (22)$$

where G_w, G_v are the transfer functions from virtual input/battery voltage to current I_b ; the output disturbance $\sigma(s)$ captures the combined impact of the additive disturbances δ_i .

Remark 1: If the battery voltage V_{bat} is measured, then a feedforward control action can be computed to compensate the impact of this disturbance in the current I_b , e.g.,

²Note that in steady state: $V_{12} \approx V_{bat}/d$ and $i_1 = -i_2$, which allows us to obtain $I_b = -w_n \frac{V_{sc}}{4dL_r \omega_s \pi}$

$w_{ff}(s) = -\frac{G_v}{G_w}V_{bat}$. On the other hand, if this measurement is unavailable, V_{bat} can be treated as an additional disturbance and included into σ .

In comparison with (14), (22) provides a reduced order, input-output linear representation of the DHB, which considerably simplifies the control design task. It also enables us to gain fundamental understanding on how the duty cycle affects the current response. For example, one can verify that the natural frequency $\omega_n(d)$ is proportional to the duty cycle, while the steady state gain $\alpha_w(d)$ is inversely proportional to d . Thus, higher duty cycles make the poles faster and decrease the converter's gain.

3) *Linear Controller*: As depicted in Fig. 6, the current controller manipulates the virtual control input w as a means to track the reference current I_b^* . It is based on a linear control law, composed of an integrator and two zeros:

$$w = C_w(s, \hat{d})e(s) = \frac{1}{\alpha_w(\hat{d})}k_c \frac{s^2 + 2\zeta_z\omega_z s + \omega_z^2}{s} e(s) \quad (23)$$

where $e(s) = I_b^*(s) - I_b(s)$ is the tracking error, C_w the transfer function of the controller, k_c the controller's gain, ω_z the natural frequency of the zeros and ζ_z their damping. The inclusion of two zeros in the controller is useful to inject damping in plants with poles that are close to the imaginary axis, such as (22) [41]. The controller also contains the term $\frac{1}{\alpha_w(\hat{d})}$ that cancels the nonlinear effect of the duty cycle in the converter's steady-state gain. Note that α_w depends on the duty cycle, which is only computed in a low-level stage by the control allocation block (see next section). To facilitate implementation, the current controller uses a predicted value of the duty cycle \hat{d} , which is estimated based on the duty cycle obtained in the previous sample time (assuming a discretized implementation of the overall controller). We rely on the controller robustness, to be discussed in detail in Section IV, to cope with the mismatch between d and \hat{d} , and to eliminate the impact of the disturbance σ .

B. Inner Loop: Control Allocation

This section presents the control allocation (CA) framework that maps w into the control action $u = (d, \phi)$. To facilitate this calculation, we consider the normalized virtual input represented as:

$$w_n = \frac{w}{V_{sc}} = \phi (4\pi d(d-1) + \phi) = g(d, \phi) \quad (24)$$

where $g(\cdot)$ is a quadratic polynomial function on d and ϕ . We assume that w_n is known and focus on inverting $g(\cdot)$ in order to find $u = (d, \phi)$. Interestingly, this inversion is not unique and there are multiple combinations of $u = (d, \phi)$ that lead to the same value of virtual input w_n . Systems with this property are known in the literature as *over-actuated* [31]. To gain insights into the over-actuation property of the converter, Fig. 8 provides a visual representation of $g(u)$ and the corresponding level curves (when $|w_n|$ is constant). One can observe that the level curves follow a quadratic pattern, which was expected due to the polynomial structure of $g(u)$. Additionally, the range of allowed duty cycle shrinks as the magnitude of w_n becomes larger.

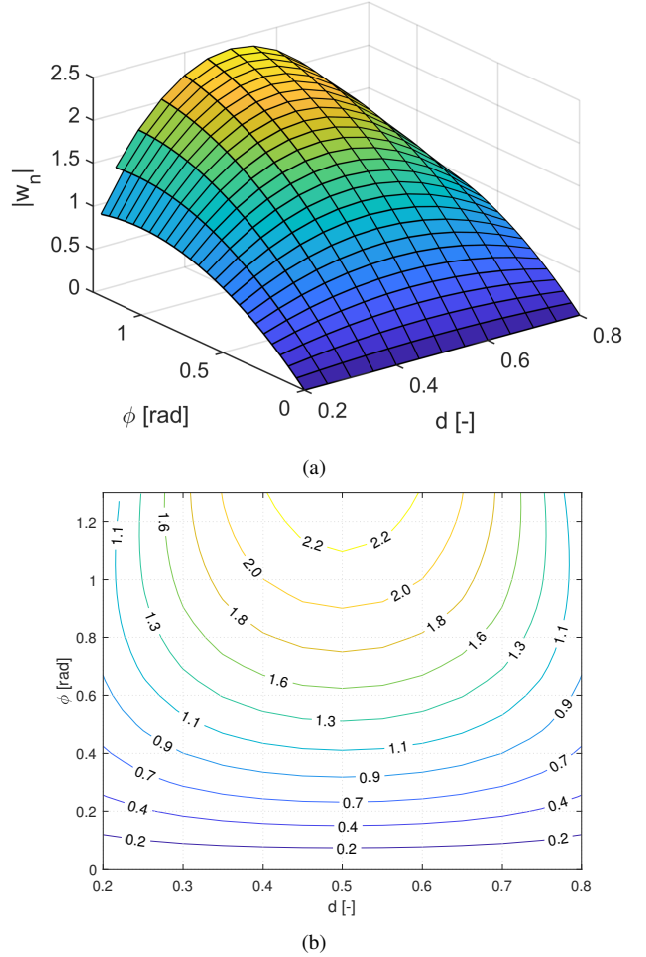


Fig. 8. a) graphical representation of the normalized virtual input w_n as function of $u = (d, \phi)$, and b) contour plots of $w_n = g(u)$.

Among the multiple of solutions for (d, ϕ) , we select the one that minimizes the current in the leakage inductor i_r , reducing the Ohmic losses in the DHB. Section II presented the detailed model of i_r , which included an analytical formula for the four operating modes of the DHB. Let us analyze i_r during the first mode $j = 1$:

$$i_r(\theta) = (v_1 + v_{sc2}) \frac{\theta}{\omega_s L_r} - i_{r0}, \quad 0 \leq \theta \leq \phi \quad (25)$$

To facilitate the integration of the i_r model into the control allocator we adopt the following assumptions:

- v_1 and v_{sc2} are approximated by their average value: $v_1 \approx (1-d)V_{12}$ and $v_{sc2} \approx dV_{sc}$; this is in line with the average modeling of the converter presented in Section II.
- the input inductor is assumed to operate in steady state and R_b is very small and can be neglected, hence $V_{12} \approx V_{bat}/d$; this approximation introduces further model approximation errors that the current controller will need to reject (see Section IV).

This allows us to express i_r as:

$$i_r(\theta) = \left(\frac{1-d}{d} + d\beta \right) V_{bat} \frac{\theta}{\omega_s L_r} - i_{r0}, \quad 0 \leq \theta \leq \phi \quad (26)$$

where $\beta = V_{sc}/V_{bat}$ is a ratio of voltages between the primary and secondary side of the DHB. Similar derivations can be made to the other operating modes of the converter ($j \in \{2, 3, 4\}$), which are omitted here due to brevity. Overall, the current in the leakage inductor will be dependent on the duty cycle d , phase shift ϕ and voltage ratio β . In this work we focus on minimizing the peak-to-peak value of i_r , i.e.

$$\|i_r(d, \phi, \beta)\|_{pp} = \max_{\theta \in [0, 2\pi]} i_r(\theta, d, \phi, \beta) - \min_{\theta \in [0, 2\pi]} i_r(\theta, d, \phi, \beta)$$

The best control action (d, ϕ) can be computed by solving the following optimization problem:

$$\mathbb{P}_1 : \min_{d, \phi} \|i_r(d, \phi, \beta)\|_{pp}^2 + k_1 \epsilon^2 \quad (27)$$

$$s.t. \quad w_n^* = g(d, \phi) + \epsilon \quad (28)$$

$$0 \leq \phi \leq 2\pi d \quad (29)$$

$$d_{min} \leq d \leq d_{max} \quad (29)$$

where w_n^* is the normalized virtual input requested by the current controller; d_{min} and d_{max} are the minimum and maximum duty cycles that the half-bridges can physically implement. The variable ϵ represents a slack variable that preserves feasibility of the problem when w_n^* is physically unattainable. The parameter k_1 is a weight defined by the designer, which should be selected high enough in order to yield small error in the allocation of w_n^* .

Note that \mathbb{P}_1 is a low-dimensional optimization problem with only two decision variables (d, ϕ) and two time-varying parameters (w_n^*, β) , allowing its optimal solution to be parameterized as $d^*(w_n^*, \beta)$ and $\phi^*(w_n^*, \beta)$. Fig. 9 illustrates these solutions, showing that ϕ^* is primarily influenced by w_n^* , while d^* is more sensitive to β . To enable real-time implementation, (d^*, ϕ^*) can be precomputed offline for a grid of (w_n^*, β) values, stored in a lookup table, and interpolated onboard a microcontroller. Finally, it is worth stressing that this work assumes DHB operation with $\phi \leq 2\pi d$, but the CA method can be extended to other modes, omitted here for brevity.

C. Control Allocation with Balancing of SC voltage

The control allocator \mathbb{P}_1 introduced in the previous section can be extended one additional goal: balancing of the voltage in the two SCs modules. In order to address this additional goal, it is useful to introduce the (normalized) voltage difference ΔV_{sc} :

$$\Delta V_{sc} = \frac{V_{sc1} - V_{sc2}}{V_{sc}} = \frac{V_{sc1} - V_{sc2}}{V_{sc1} + V_{sc2}} = 1 - 2d \quad (30)$$

Note that, since the voltage difference ΔV_{sc} is directly affected by the d , the DHB's duty cycle is a suitable control input for balancing purposes. The goal of the SC balancing task is to bring ΔV_{sc} to zero. To define how fast the ΔV_{sc} should converge to zero, we employ the following first-order reference dynamic system:

$$\tau_{eq} \frac{d\Delta V_{sc}^*}{dt} = -\Delta V_{sc}^*, \quad \Delta V_{sc}^*(0) = \Delta V_{sc}(0) \quad (31)$$

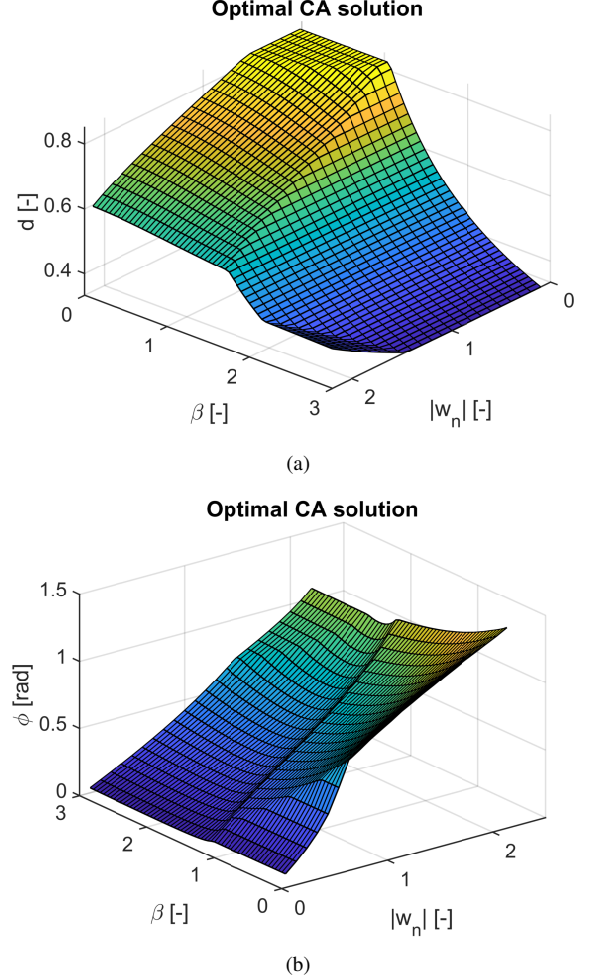


Fig. 9. Representation of the optimal solutions (d^*, ϕ^*) for the control allocation problem \mathbb{P}_1 . Note that $\beta = V_{sc}/V_{bat}$.

where τ_{eq} is the desired decay time for equalization and ΔV_{sc}^* the desired voltage difference. Solving this first-order differential equation leads to

$$\Delta V_{sc}^*(t) = \Delta V_{sc}(0)e^{-t/\tau_{eq}} \quad (32)$$

This yields a reference value for ΔV_{sc}^* that exponentially decays to zero. Let us consider $d_b(t)$ as the reference duty cycle to track the reference dynamic system³. Combining this reference dynamics with (30) allows us to obtain a closed-form expression for the reference duty cycle:

$$d_b(t) = \frac{1}{2} - \frac{\Delta V_{sc}(0)}{2} e^{-t/\tau_{eq}} \quad (33)$$

$$= \frac{1}{2} - \frac{V_{sc1}(0) - V_{sc2}(0)}{2(V_{sc1}(0) + V_{sc2}(0))} e^{-t/\tau_{eq}} \quad (34)$$

This algorithm acts as a soft-start strategy for gradual SC voltage balancing. Initially, the duty cycle $d_b(0)$ compensates for voltage imbalances; then it slowly converges to the steady-state value ($d_{ss} = 1/2$). A sufficiently large τ_{eq} prevents surge power transients during initialization.

³Recall that, from (30) we have $\Delta V_{sc}^*(t) = 1 - 2d_b$

The balancing duty cycle d_b can be incorporated into the CA problem via an additional cost term that promotes attraction of d towards d_b :

$$\begin{aligned} \mathbb{P}_2 : \quad & \min_{d,\phi} \|i_r(d,\phi,\beta)\|_{pp}^2 + k_1\epsilon^2 + k_2\|d - d_b\|^2 \\ s.t. \quad & w_n^* = g(d,\phi) + \epsilon \end{aligned} \quad (35)$$

$$0 \leq \phi \leq 2\pi d \quad (36)$$

$$d_{min} \leq d \leq d_{max} \quad (37)$$

where k_2 is a weight factor, defined by the designer, which stimulates convergence of d to d_b .

An analytical solution can be computed for \mathbb{P}_2 via inversion of the quadratic mapping (35). Assuming that the inequalities are inactive in \mathbb{P}_2 , w_n^* is attainable (i.e. $\epsilon = 0$) and $k_2 \rightarrow \infty$, two candidate solutions exist:

$$\phi^* = 2\pi d_b(1 - d_b) \pm \sqrt{(2\pi d_b(1 - d_b))^2 + w_n^*}, \quad d = d_b \quad (38)$$

From these two candidate solutions we pick the one that minimizes $\|i_r\|_{pp}^2$.

Remark 2: The design of the current controller and the control allocation \mathbb{P}_1 are generic and can be applied to any DHB converter. The control allocation \mathbb{P}_2 is more specific and assumes that the secondary side of the dual half bridge is connected to multiple (super)capacitors.

D. Practical Considerations

This section presents a short discussion on practical issues for the DHB implementation including: i) robustness of the controller against model uncertainties; ii) enforcement of lower/upper limits in V_{sc} , V_{12} and iii) initialization with zero voltage.

1) *Robustness:* The proposed control algorithm relies on the accuracy of the simplified nonlinear model (14d), which approximates the behavior of the DHB. Since this model involves simplifications, concerns may arise regarding the ability of the nonlinear inversion (38) and the linear control law (23) to preserve stability in the presence of model uncertainties.

The nonlinear inversion of the DHB model is robust against parameter variations. This robustness stems from the fact that (38) depends primarily on control inputs (d_b) and the normalized virtual input w_n^* , which, in turn, depends on the supercapacitor voltage (V_{sc})—a quantity that is usually measured with high accuracy. Consequently, the nonlinear inversion is not sensitive to variations in the DHB's physical parameters (e.g., L_b, C_b, C_{sc}), which may be uncertain and subject to drift over time.

On the other hand, the linear current control law is more susceptible to model uncertainties. To address this, Section IV provides a detailed analysis on how to tune the controller's gains (k_c, ω_z, ζ_c) to ensure robustness against model mismatches of up to 300%. Furthermore, Section V validates the effectiveness of the proposed control strategy through simulations using a high-fidelity DHB model that incorporates dynamics neglected in the simplified model used for control design.

2) *Voltage Constraints:* The control strategy discussed so far does not limit the value of the voltages V_{12} and V_{sc} . In practice, it would be useful to compute control actions that avoid violation of under- or over-voltage constraints. Interestingly, our control allocation framework can be easily extended to deal with these safety constraints. To understand this, let us first discretize (16c) with the Euler approximation:

$$\frac{dV_{sc}}{dt} \approx \frac{V_{sc}[k+1] - V_{sc}[k]}{T_s} = l(V_{12}, V_{sc})w \quad (39)$$

where $l(V_{12}, V_{sc}) = -\frac{1}{2C_{sc}L_r\omega_s\pi}\frac{V_{12}}{V_{sc}}$ and T_s is the sampling time and k the discrete time index. This approximation allows us to predict the supercapacitor voltage at the next time step as:

$$V_{sc}[k+1] = V_{sc}[k] + T_s l(V_{12}, V_{sc})w \quad (40)$$

To prevent overvoltage conditions at the next time step, we would need to enforce $V_{sc}[k+1] \leq V_{sc}^{max}$, where V_{sc}^{max} is the maximum allowed voltage. This requirement could be easily included as an additional constraint in the control allocation problems \mathbb{P}_1 and \mathbb{P}_2 , leading to (recall that $w = V_{sc}(w_n^* - \epsilon)$):

$$V_{sc}[k] + T_s l(V_{12}, V_{sc})V_{sc}(w_n^* - \epsilon) \leq V_{sc}^{max} \quad (41)$$

where ϵ is a correction value computed by the control allocation in order to fulfill all constraints. A similar approach could be followed in order to deal with undervoltage conditions (and also under/overvoltage constraints in V_{12}).

3) *Initialization with Zero Voltage:* The inversion of the virtual input (24) is not well defined at $V_{sc} = 0$. This singularity may occur during the startup of the DHB with zero capacitor voltage. In order to deal with this issue, the following two-phase startup sequence can be applied:

- Phase 1 involves charging the primary capacitors (C_b). To limit the inrush inductor current I_b , it is advisable to include a pre-charge-resistor and set $\phi = 0$ rad (which leads to $w_n = 0$ and prevents power flow to the secondary side of the DHB).
- Phase 2 focuses on increasing the voltage V_{sc} , which can be achieved by slowing increase i_3 in the equivalent circuit represented in Fig. 7. This can be obtained with a small phase shift ϕ and a constant duty cycle d , leading to a small w_n (and charging current i_3).

Once V_{sc} achieves an acceptable minimum level, the current controller and control allocation presented in this Section can be enabled.

IV. ANALYSIS OF THE CURRENT CONTROLLER

This section analyses in more detail the tuning of the high-level current controller introduced in Section III-A.

A. Control Specifications

The tuning of the current controller focuses on the selection of (k_c, ζ_c, ω_c) , capable of fulfilling numerous transient, disturbance rejection and robustness requirements. To facilitate this process, we fix the damping of the controller's zeros ($\zeta_c = 0.707$) and focus on the tuning of the remaining

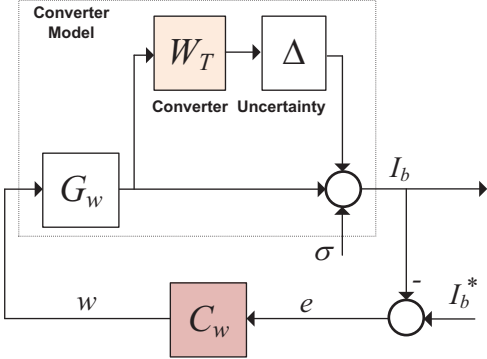


Fig. 10. Representation of the converter's unstructured uncertainty (Δ) and disturbance (σ).

TABLE II
SPECIFICATIONS OF THE CURRENT CONTROLLER.

Parameter	Symbol	Value
max. real pole	$\bar{\alpha}$	$-2\pi 20 \text{ rad/s}$
low-frequency model uncertainty	l_T	0.5
high-frequency model uncertainty	h_T	3
cross-over frequency for model uncertainty	ω_T	$1.6 \omega_n(d)$
low-frequency disturbance attenuation	$M_{\sigma 2}$	5×10^{-5}
high-frequency disturbance attenuation	$M_{\sigma 1}$	2
cross-over frequency for W_S	ω_S	$2\pi 20 \text{ rad/s}$

parameters $q = [k_c, \omega_z]^T$. It is assumed that these tuning parameters are lower/upper bounded:

$$Q = \{q = [k_c, \omega_z]^T : k_c \in [0, k_c^{max}], \omega_z \in [0, \omega_z^{max}]\} \quad (42)$$

where $k_c^{max}, \omega_z^{max}$ are pre-defined maximum values.

The first specification of the current controller focuses on pole placement. It can be formulated using the closed-loop transfer function of the converter:

$$I_b(s, q) = \frac{G_w(s)C_w(s, q)}{1 + G_w(s)C_w(s, q)} I_b^*(s) = T(s, q) I_b^*(s) \quad (43)$$

and its characteristic polynomial:

$$\begin{aligned} p(s, q) &= \text{num}\{G_w(s)C_w(s, q)\} + \text{den}\{G_w(s)C_w(s, q)\} \\ &= k_c \omega_n^2(d) (s^2 + 2\zeta \omega_z s + \omega_z^2) + (\omega_n^2(d) + s^2) \end{aligned} \quad (44)$$

where $\text{num}(\cdot)$ and $\text{den}(\cdot)$ correspond to numerator and denominator of a transfer function, respectively and $T(s, q)$ is the complementary sensitivity function of the converter. The roots of p define the closed-loop poles, which directly affect the transient response of the converter. We focus on the dominant behavior of the converter and specify that the real part of all (closed-loop) poles should be lower than $\bar{\alpha} < 0$; this forces all the converter's modes to exponentially decay like $e^{-|\bar{\alpha}|t}$ [28].

The set of tuning parameters that fulfill this specification is defined as:

$$\mathcal{Q}_p = \{q \in Q : \text{Re}(\text{roots}\{p(s, q)\}) \leq \bar{\alpha}\} \quad (45)$$

where $\text{roots}(\cdot)$ is a function that returns the roots of the characteristic polynomial, and $\text{Re}(\cdot)$ extracts the real part.

The second control specification focus on rejecting the output disturbance σ . The effect of this disturbance (as well

as the reference signal I_b^*) in the controller's tracking error is given as:

$$e(s, q) = \frac{1}{1 + G_w(s)C_w(s, q)} (I_b^*(s) - \sigma(s)) = \quad (46)$$

$$= S(s, q)(I_b^*(s) - \sigma(s)) \quad (47)$$

where $S(s, q)$ is known as the sensitivity function. The controller should guarantee that the disturbances have a low impact in the traction error, i.e., $|S(j\omega, q)| \leq M(j\omega)$ over a frequency range of interest, where $M(j\omega)$ represents the desired level of disturbance attenuation. This requirement can be re-formulated using the ∞ -norm operator [42]:

$$\|W_S(s)S(s, q)\|_\infty = \sup_\omega |W_S(j\omega)S(j\omega, q)| \leq 1 \quad (48)$$

where $W_S(s) = M(s)^{-1}$ is the inverse of the desired disturbance attenuation profile, defined in this work as

$$W_S(s) = \frac{\frac{s}{M_{\sigma 1}} + \omega_\sigma}{s + \omega_\sigma M_{\sigma 2}} \quad (49)$$

with $M_{\sigma 1}$ representing the high-frequency attenuation, $M_{\sigma 2}$ the low-frequency attenuation level and ω_S a cross-over frequency. The set of tuning parameters that fulfill the disturbance attenuation specification is captured by the following set:

$$\mathcal{Q}_S = \{q \in Q : \|W_S(s)S(s, q)\|_\infty \leq 1\} \quad (50)$$

The third specification ensures robustness against unstructured uncertainty from non-modeled dynamics and parameter variations. For instance, (16) neglects parasitic elements and uses practical approximations that simplify controller design but introduce modeling errors (denoted as σ in the previous section). Additionally, physical parameters in the converter (e.g., inductance, capacitance) vary with temperature and aging, causing further model mismatches. At low frequencies ($\omega \ll \omega_n$), the converter's transfer function can be approximated as:

$$I_b(j\omega) \approx \alpha_w(d) w(j\omega) = \frac{1}{4L_r \omega_s \pi d} w(j\omega) \quad (51)$$

This formula reveals that the leakage inductance L_r is a key parameter in the low-frequency response; it is also a physical parameter with high level of uncertainty (up to 15% according to [43]). At higher frequencies, other physical parameters (e.g. input inductance and capacitance) play a more predominant role. To account for this model uncertainty, we assume that the modeling mismatch introduce an unstructured multiplicative uncertainty in (22), characterized by

$$G_w(s)(1 + W_T(s)\Delta(s)) \quad (52)$$

where W_T represents a frequency-dependent uncertainty profile and Δ a multiplicative uncertainty satisfying $\|\Delta\|_\infty \leq 1$ (see Fig. 10)). By direct application of the small-gain Theorem, robustness against this uncertainty can be ensured as long as [28]

$$\|W_T(s)T(s, q)\|_\infty \leq 1. \quad (53)$$

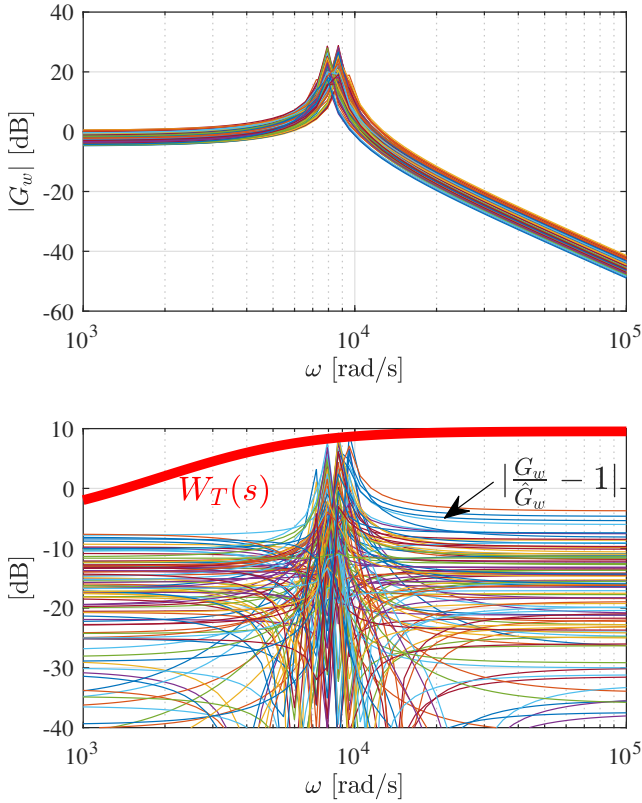


Fig. 11. Top plot: Frequency response of the converter model G_w with parametric uncertainty ($\pm 30\%$ uncertainty in L_r , $\pm 20\%$ in R_b and $\pm 10\%$ in L_b and C_1, C_2). Bottom plot shows $W_T(s)$ and the normalized modeling error profile $|G_w / \hat{G}_w - 1|$, where \hat{G}_w is the nominal transfer function of the converter (i.e., with nominal parameters).

B. Model Uncertainty

To assess DHB model uncertainty, Fig. 11 shows the frequency response of the ideal transfer function G_w under parametric variations. The plot includes 200 curves generated using uniformly distributed parameter variations: $\pm 30\%$ in L_r , $\pm 20\%$ in R_b , and $\pm 10\%$ in L_b, C_1 , and C_2 . To visualize model mismatch, the bottom plot in Fig. 11 presents the normalized modeling error $|G_w / \hat{G}_w - 1|$, where \hat{G}_w is the nominal transfer function (i.e., with nominal parameters). The results show errors ranging from -7 dB at low frequencies, peaking at 8 dB near the natural frequency, and reducing to -4 dB at higher frequencies. The bottom plot also illustrates the uncertainty profile W_T , which defines a worst-case uncertainty envelope for the DHB simplified model, parameterized as:⁵

$$W_T(s) = h_T \frac{s + \omega_T l_T}{s + \omega_T h_T} \quad (54)$$

where l_T, h_T represent the (relative) model uncertainty at low and high frequencies, respectively, and ω_T the crossover frequency. The set of controller gains that fulfills the robustness specification is defined as:

$$\mathcal{Q}_T = \{q \in Q : \|W_T(s)T(s, q)\|_\infty \leq 1, \} \quad (55)$$

Table II contains the values of the specifications employed in this work.

C. Tuning via Parameter Space

The controller synthesis is the last step in the design of the current controller. The aim is to find the set of control parameters (k_c, ω_z) that fulfill the specifications described in the previous sub-section, i.e., the set

$$\mathcal{Q}^* = \mathcal{Q}_p \cap \mathcal{Q}_S \cap \mathcal{Q}_T \quad (56)$$

To compute this set, we employ the parameter space approach (PSA) [28] and an adapted version of the Matlab PARADISE toolbox [44]. The computation process works as follows:

- \mathcal{Q}_p : Let Γ be the desired closed-loop pole region, defined in the complex plane as $\Gamma = \{s \in \mathbb{C} : \text{Re}\{s\} \leq \bar{\alpha}\}$, with boundary $\partial\Gamma = \{s \in \mathbb{C} : s = \bar{\alpha} + j\omega, \omega \in \mathbb{R}\}$. The closed-loop poles lie on this boundary if $p(\bar{\alpha} + j\omega, q) = 0$ for some $\omega \in \mathbb{R}$. Since this equation uses complex numbers, it can be separated into two real-valued equations:

$$p_1(\omega, q) = \text{Re}\{p(\bar{\alpha} + j\omega, q)\} = 0 \quad (57a)$$

$$p_2(\omega, q) = \text{Im}\{p(\bar{\alpha} + j\omega, q)\} = 0 \quad (57b)$$

where Im extracts the imaginary component of a complex number. If we assume that $\omega = \omega_0$ is fixed, then we obtain two nonlinear polynomial equations with two unknowns ($q \in Q \subset \mathbb{R}^2$). The solutions for these equations⁴ represents control parameters that place closed-loop poles on $\partial\Gamma$. The PSA method maps $\partial\Gamma$ to the parameter space Q by sweeping ω and solving (57), constructing the boundary:

$$\partial\mathcal{Q}_P = \{q \in Q : p(\bar{\alpha} + j\omega, q) = 0, \omega \in \mathbb{R}\} \quad (58)$$

The boundary may define candidate regions $\mathcal{Q}_j, j \in \{1, \dots, n\}$ for fulfillment of pole-placement specification. To verify $\mathcal{Q}_j \subset \mathcal{Q}_P$, we evaluate a test point $q^* \in \mathcal{Q}_j$: if q^* places closed-loop poles inside Γ , then by the boundary crossing theorem [28], the entire region \mathcal{Q}_j belongs to \mathcal{Q}_P .

- \mathcal{Q}_S : fulfillment of the disturbance rejection specification (48) can be expressed as $|S(j\omega, q)| \leq |W_S^{-1}(j\omega)|, \forall \omega \in \mathbb{R}$. Similarly to the pole-placement specification, we can also define a region in the frequency-response plane where the disturbance rejection specification is fulfilled:

$$\mathcal{B}(\omega) = \{B \in \mathbb{R} : B \leq |W_S^{-1}(j\omega)|\} \quad (59)$$

and then map the boundary of this set ($\partial\mathcal{B}(\omega)$) to the control parameter space [28]:

$$\partial\mathcal{Q}_S = \{q \in Q : |S(j\omega, q)| = \partial\mathcal{B}(\omega), \omega \in \mathbb{R}\} \quad (60)$$

The boundary defines candidate regions for \mathcal{Q}_S within the Q plane. By the mean value theorem [28], if a test point q^* in a candidate region satisfies the disturbance-rejection specification, the entire region belongs to \mathcal{Q}_S .

- \mathcal{Q}_T : the construction of this last set is analogous to \mathcal{Q}_S , but using $T(s, q)$ and $W_T(s)$ instead of $S(s, q)$ and $W_S(s)$.

⁴note that (57) might have no solutions, one solution or multiple solution [28]

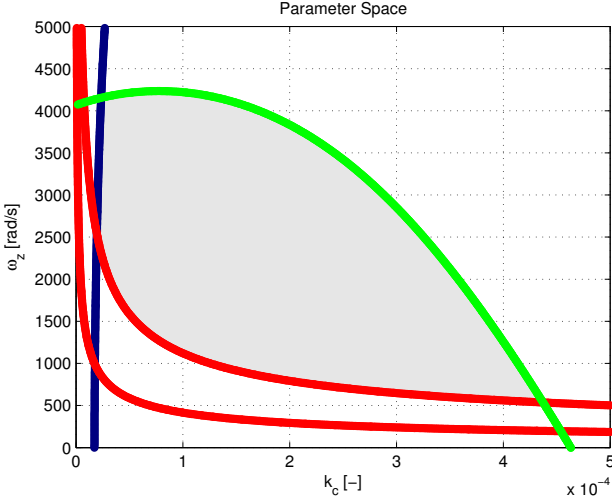


Fig. 12. Boundaries of the parameter space: red lines are linked with disturbance rejection boundary $\partial\mathcal{Q}_S$; blue with boundary of the pole-placement specifications, $\partial\mathcal{Q}_P$ and green with robustness boundary $\partial\mathcal{Q}_T$. Gray area represents the set of parameters that fulfill all specifications (\mathcal{Q}^*).

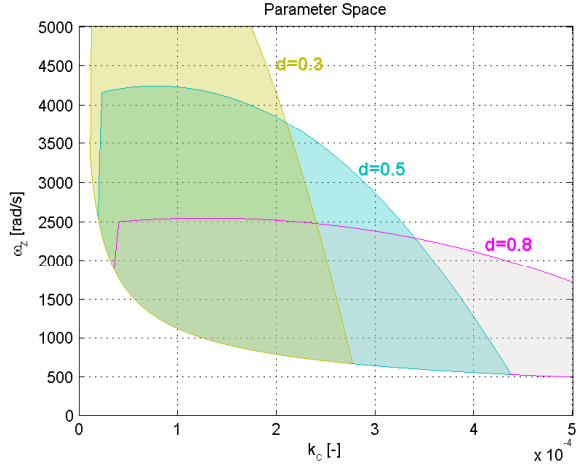


Fig. 13. Effect of the duty cycle d in the allowed set of controller parameters.

D. Analysis and Discussion

Fig. 12 shows the boundaries $\partial\mathcal{Q}_P$, $\partial\mathcal{Q}_S$, $\partial\mathcal{Q}_T$ in the plane (k_c, ω_z) , as well as the set \mathcal{Q}^* that fulfills all the specifications. These results reveal that the pole-placement specification (blue line) introduces a lower bound on the parameter k_c ; this means the controller's gain needs to be sufficiently high enough to meet the pole-placement specifications. The robustness specification (green line) limits the maximum value of ω_z as a function of k_c . It shows an inherent trade-off in the controller tuning: higher gains (k_c) reduce the maximum value of the controller's zeros (ω_z); in fact, for $k_c > 4.7 \times 10^{-4}$ it is impossible to fulfill all the controller specifications. We can conclude that, high controller gain (k_c) and high zero (ω_z) will compromise robustness. One can also observe that the disturbance rejection specification (red lines) enforces a lower bound on (ω_z), which decreases exponentially with k_c .

Fig. 13 depicts the effect of the duty cycle in the allowed set of controller gains (k_c, ω_z) . The results show higher duty

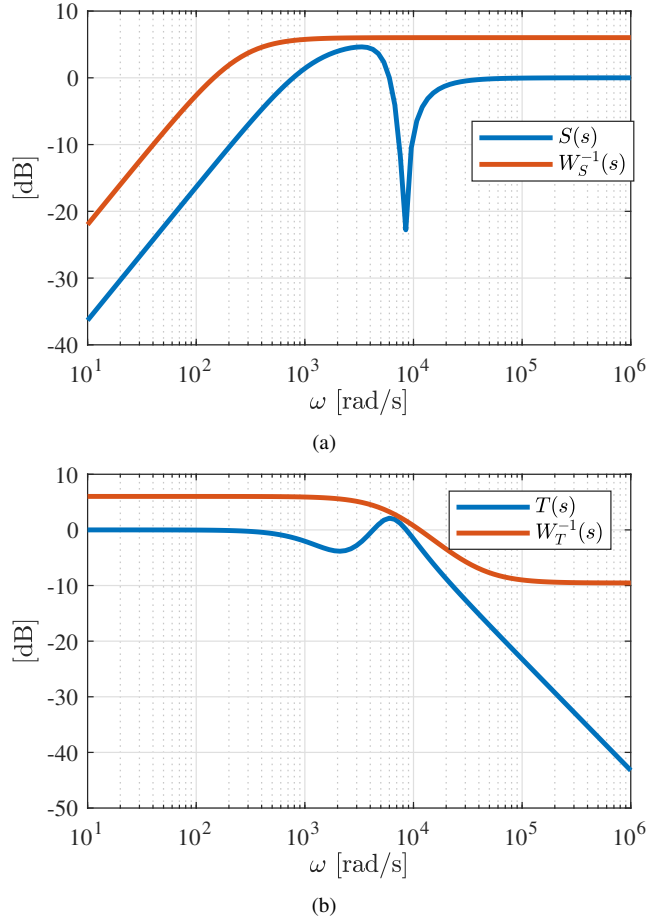


Fig. 14. Frequency response of the sensitivity ($S(s)$) function, complementary sensitivity ($T(s)$), and the inverse of the weight functions ($W_S^{-1}(s)$, $W_T^{-1}(s)$). These results demonstrate fulfillment of the design constraints $|S(j\omega)| \leq |W_S(j\omega)|^{-1}$, $|T(j\omega)| \leq |W_T(j\omega)|$

cycles increase the minimum value for k_c and decrease the maximum allowed ω_z . In other words, high duty cycles move the allowed set of gains down and right in the (k_c, ω_z) -plane. Interestingly, there is an overlap of allowed set of gains for different values of d , which allows us to employ constant values of (k_c, ω_z) to fulfill the control specifications.

Fig. 14 shows the frequency response of several transfer functions (sensitivity ($S(s)$)) function, complementary sensitivity function ($T(s)$) and weight functions ($W_S(s)$, $W_T(s)$) for one of the candidate parameter $q = (k_c, \omega_z) = (0.5 \times 10^{-4}, 2560) \in \mathcal{Q}^*$. The obtained results demonstrate that the sensitivity (complementary sensitivity) functions are below $W_S(s)$ (W_T), which verifies compliance with disturbance rejection and robustness specifications⁵.

V. SIMULATION RESULTS

The proposed nonlinear controller was validated via numerical simulations with the switching model of the DHB presented in Section II. Appendix A contains the parameters of the controller employed in the numerical simulations.

⁵note that $\|W_S(j\omega)S(j\omega)\|_\infty \leq 1$ is equivalent to $|S(j\omega)| \leq |W_S^{-1}(j\omega)|$ for all $\omega \geq 0$.

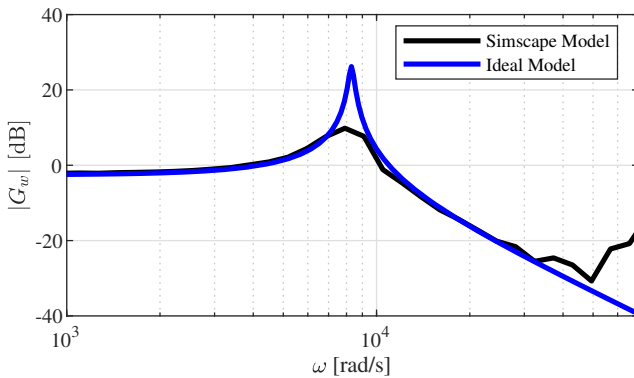


Fig. 15. Frequency response of the DHB converter, $G_w(s) = I_b(s)/w(s)$, obtained with the ideal model (blue curve) and the high-fidelity model implemented in Matlab Simscape (black curve).

A. Modeling Mismatch

The *simulation model* of the DHB was implemented in Matlab-Simscape, which provides a DHB model with a higher degree of fidelity than the *reduced-order model* (16). This *simulation model* considers parasitic losses in the capacitors and inductors, pulse-width modulation, and switching of the power semiconductors, which were neglected in the *reduced-order model*. Fig. 15 depicts the frequency response of G_w obtained with the i) *reduced-order model* (also referred as ideal model in the sequel) and ii) the Simscape *simulation model*. The results reveal a good match between the two models at low frequencies. There are two frequency regions where significant model mismatches are observed. The first is around the natural frequency of the converter (ω_n): the ideal model predicts a resonant peak that is significant higher than the one observed with the high-fidelity model; this can be explained by parasitic losses in the high-fidelity model, which increase damping. The second model mismatch occurs at higher frequencies due to non-modeled dynamics. The DHB control algorithm, which was designed in the previous section with robust synthesis techniques, needs to cope with this model mismatch.

B. Transient Response

The first batch of tests evaluate the transient benefits of the proposed nonlinear control strategy. To demonstrate this, we benchmark two controllers:

- *baseline linear controller*, which consider the linearization of the DHB model (14) around the equilibrium point ($d^{eq} = 0.5$, $\phi^{eq} = 0$, $V_{sc}^{eq} = 4V$). This linear controller has the same structure as the (23) and was parameterized with similar closed-loop specifications (in terms of pole-placement, disturbance rejection and robustness). This type of controller has been employed in the previous literature, such as [12].
- *nonlinear controller*, composed of the current controller (23) and the control allocation \mathbb{P}_2 (operating with a fixed duty cycle).

Fig. 16 shows the result for a step change in the current setpoint with a duty cycle $d = 0.5$. One can observe that both linear and nonlinear controllers provide similar responses.

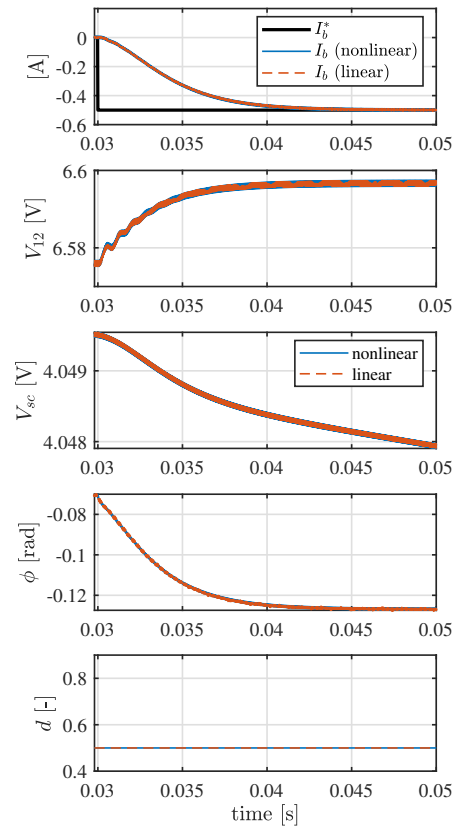


Fig. 16. Numerical validation of the current controller: step response with duty cycle $d = 0.5$.

In this test case, the linear controller operates close to the equilibrium point used in the linearization and where the linear model approximation is accurate. Since both linear and nonlinear controllers have similar specifications, this similarity in transient performance was expected since the modeling errors are small.

Fig. 17 presents the results when the current controllers operate with a duty cycle $d = 0.85$. The results reveal that the transient performance of the linear controller degrades significantly in comparison with the nonlinear approach. In this case, the linear controller operates further away from the equilibrium point employed in the linearization. Hence, larger modeling errors are introduced, which significantly degrade the transient performance of the linear controller. In contrast, the response of the nonlinear controller remains largely unaltered by the new operating point of the converter. In this particular case, the linear controller relies on integration action to recover zero tracking error. This happens because the nonlinearity decreases the plant's gain; thus the integral action of the linear controller has to compensate for this loss of gain, leading to a slower response.

Let us now analyze in more detail the effect of the duty cycle in the controller's performance, in particular its settling time. Fig. 18 depicts the controllers' settling time for different values of duty cycle when a step change in the current setpoint is applied. Both controllers provide a similar level of performance for duty cycles up to 0.6. For larger duty cycles, the settling time of the linear controller increases significantly

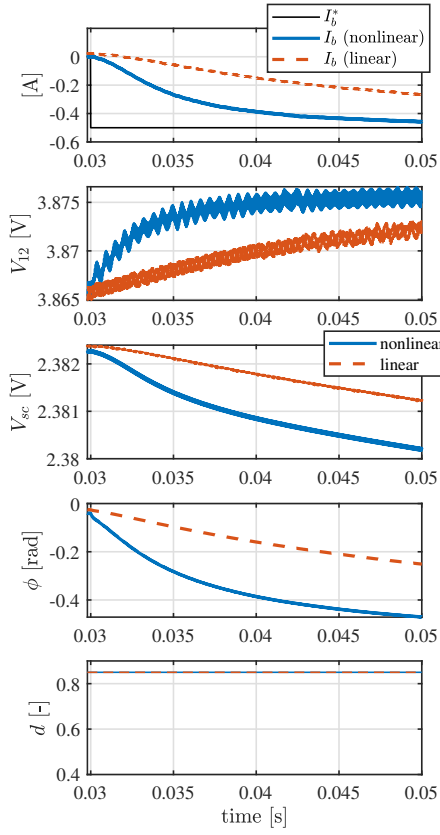


Fig. 17. Numerical validation of the current controller: step response with $d = 0.8$.

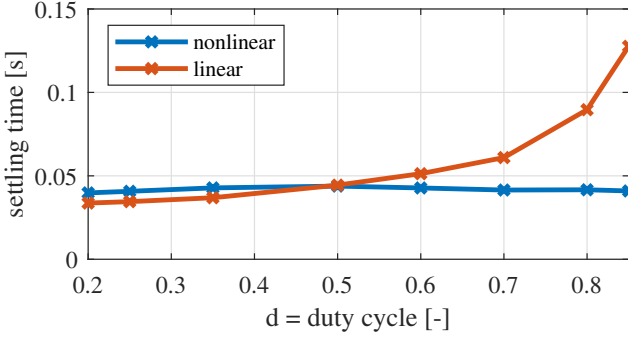


Fig. 18. Settling time of the current controller (within a 2% error bound) for a step change in the current reference ($I_b^* = 0.5\text{A}$).

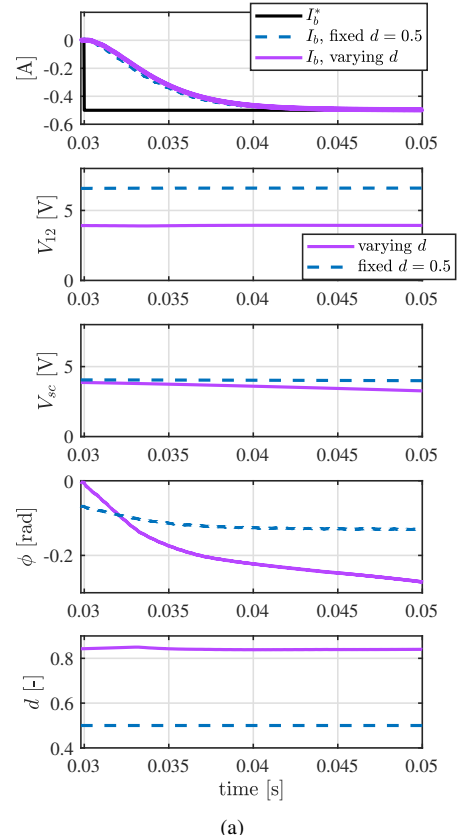
(because of larger modeling errors), while the response of the nonlinear controller remains unaffected.

C. Control Allocation Without Voltage Balancing

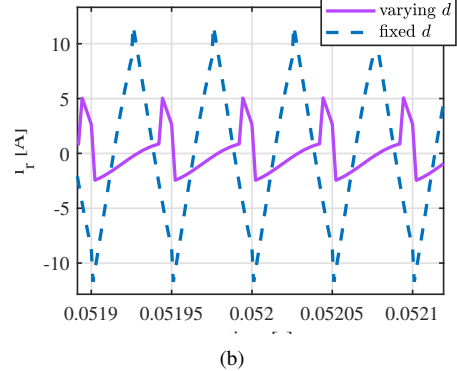
The second test focuses on evaluating the ability of the control allocation to minimize the transformer current i_r . To demonstrate this, we benchmark two control allocation strategies:

- \mathbb{P}_1 with variable duty cycle.
- \mathbb{P}_2 with fixed duty cycle. $d = d_b = 0.5$.

Fig. 19 provides an overview of the obtained results. One can observe that both controllers \mathbb{P}_1 and \mathbb{P}_2 generate similar current response (I_b), despite having very different control



(a)



(b)

Fig. 19. Time-domain comparison of different control allocation strategies, with varying duty cycle (\mathbb{P}_1) and fixed duty cycle (\mathbb{P}_2 with $d = 0.5$)

actions (d, ϕ) . The main difference lies in the transformer current i_r . Using fixed duty cycle ($d = 0.5$), the peak to peak value of the current reaches approximately 23.2A, while the varying duty cycle reduces the peak-to-peak value to 7.5A (a 67% reduction).

The current reduction provided by time varying duty cycle (formulation \mathbb{P}_2) depends on the operating point of the DHB (β, ω_n) . To better quantify the potential gains, Fig. 20 depicts ratio:

$$\chi = \frac{\|i_r(\mathbb{P}_1)\|_{pp}}{\|i_r(\mathbb{P}_2)\|_{pp}} \quad (61)$$

a normalized performance indicator that allow us to compare the peak-to-peak i_r current for fixed and varying duty cycles. These results reveal the current reduction offered by varying duty cycle is more pronounced when low levels of virtual

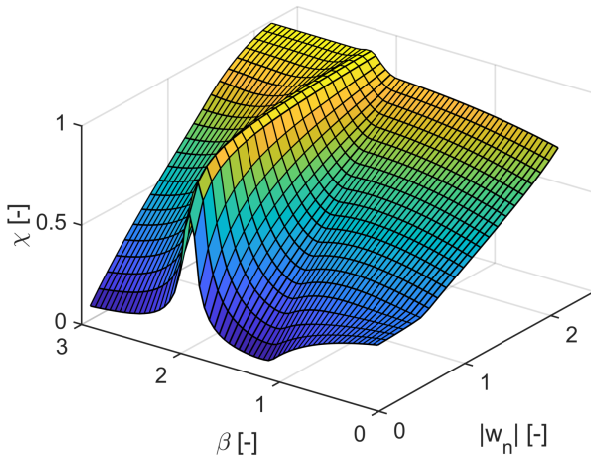


Fig. 20. Normalized transformer current χ , obtained with varying duty cycle (\mathbb{P}_1) and fixed duty cycle (\mathbb{P}_2 with $d = 0.5$). Note: $\chi = \frac{\|i_r(\mathbb{P}_1)\|_{pp}}{\|i_r(\mathbb{P}_2)\|_{pp}}$.

input w_n^* are requested; in this region, peak-to-peak current reduction of up 80% are possible.

D. Control Allocation With Voltage Balancing

The third test case focuses on validating the SC balancing, while following repetitive stepwise I_b^* profile. We use the control allocation \mathbb{P}_2 with a fixed duty cycle computed from the balancing algorithm (34). The test considers a significant initial imbalance in the SC voltages ($V_{sc1}(0) = 0.85V$, $V_{sc2}(0) = 2V$), which might appear due to differences in the self-discharge rates of the SCs. As depicted in Fig. 21, the SC balancing algorithm initializes the converter's duty cycle to match the initial voltage in the SCs ($d = 0.7$). Afterwards, the balancing algorithm slowly decreases the duty cycle d in order to equalize the SC voltage, which is successfully achieved after 20s.

It is also interesting to note that the phase shift magnitude ϕ increases significantly at higher duty cycles. For instance, at the start of the test, $\phi = 0.8$ rad is needed to maintain 3A input current with $d = 0.7$, whereas by the end, only $\phi = 0.38$ rad is required for $d = 0.5$. This strong duty-cycle–phase-shift coupling in the DHB underscores the need for nonlinear control to effectively compensate for these interactions. Another key design factor is the equalization time t_{eq} . Smaller t_{eq} values speed up SC equalization but increase surge currents. As shown in Fig. 22, when $t_{eq} < 5s$, SC root-mean-square current rises sharply (up to 500%), leading to higher energy losses. For the configuration used in this study, $t_{eq} > 10s$ is preferable.

VI. CONCLUSION AND OUTLOOK

We proposed a nonlinear framework for controlling dual half-bridge power converters. This framework employed input-output linearization methods to track current and a control allocator that strategically selects the converters' duty cycle and phase shift to minimize Ohmic losses and to balance voltages in the converter's secondary side. The ability to cancel the dominant nonlinearities in the converter represents

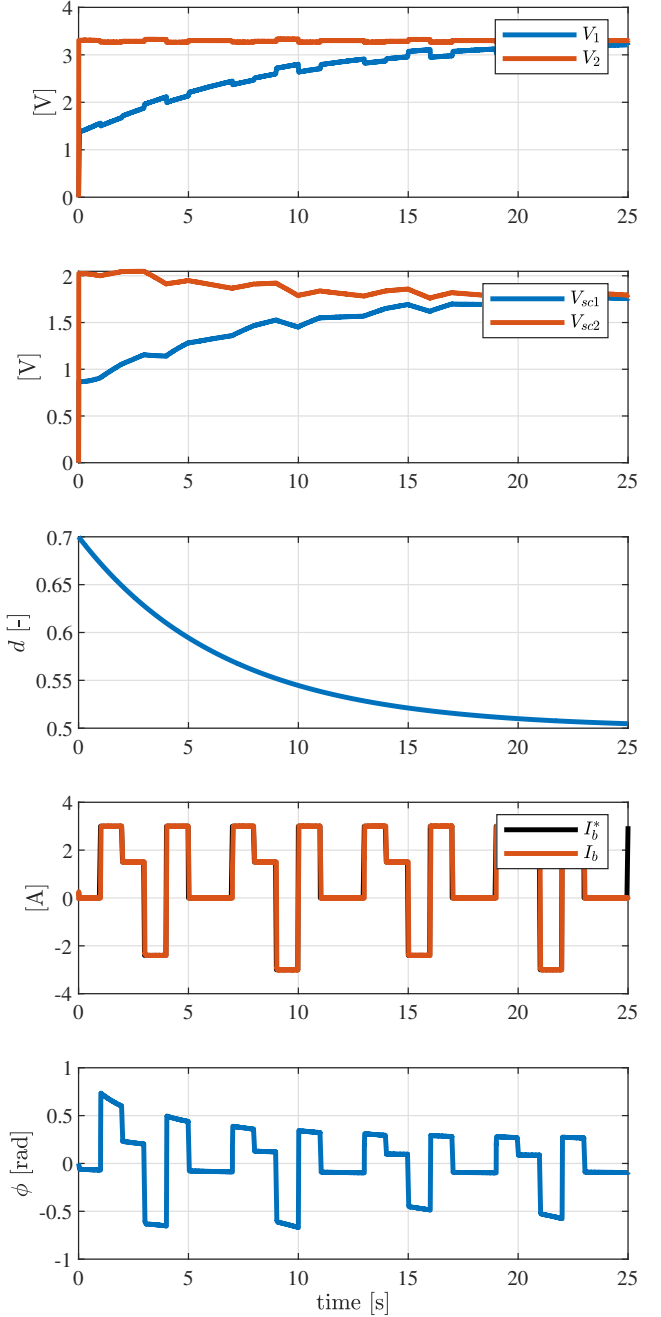


Fig. 21. Numerical validation of the balancing algorithm for the SC voltage.

one of the key advantages offered by the proposed approach, facilitating the control design task. This control framework was then applied to regulate power flow in a hybrid energy storage system comprising a battery pack and supercapacitors. The obtained simulation results demonstrated that, in comparison to linear control methods, the nonlinear control framework provides superior settling time of the current loop over a wide range of operating conditions. It also offers a practical mechanism to reduce in up to 80% the peak-to-peak current in the DHB's transformer.

Future work will focus on the experimental validation of the nonlinear control framework. We also aim to develop fault estimators to improve reliability of DHB power converters and

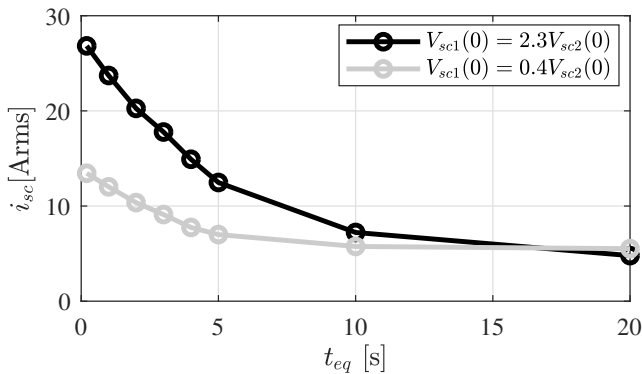


Fig. 22. Average root-mean-square (rms) current in the SCs for different initial conditions.

sampled-data modeling frameworks to improve accuracy of the DHB model.

APPENDIX

A. Converter and ESS Parameters

The parameters employed in the DHB and controller are as follows. ESS: $v_{bat} = 3.3V$, $C_{sc1} = C_{sc2} = 0.350F$, DHB: $R_b = 10m\Omega$, $L_b = 33\mu H$, $C_1 = C_2 = 0.220mF$, $L_r = 1.7\mu H$, $\omega_s = 2\pi 20kHz$, Control: $k_c = 0.5 \times 10^{-4}$, $\omega_z = 2560$ rad/s.

B. DHB Average Model

The auxiliary matrices of the DHB model (10) are defined as:

$$\begin{aligned} A_{sx}(u)X &= \frac{1}{T_s} \sum_{j=1}^4 \int_{t_j}^{t_{j+1}} (A_{sx}^j X + A_{sr}^j i_r^*(t, X)) dt \\ A_{sm}(u) &= \frac{1}{T_s} \sum_{j=1}^4 \int_{t_j}^{t_{j+1}} A_{sm}^j dt \\ B_s(u) &= \frac{1}{T_s} \sum_{j=1}^4 \int_{t_j}^{t_{j+1}} B_s^j dt \\ A_{mx}(u) &= \frac{1}{T_s} \sum_{j=1}^4 \int_{t_j}^{t_{j+1}} A_{mx}^j dt \end{aligned} \quad (68)$$

Fig. (23) contains the closed-form expression for these matrices, which were obtained using Matlab Symbolic Toolbox.

REFERENCES

- [1] Z. Dai, H. Liu, M. O. Rodgers, and R. Guensler, "Electric vehicle market potential and associated energy and emissions reduction benefits," *Appl. Energy*, vol. 322, p. 119295, Sep. 2022.
- [2] M. Rouholamini, C. Wang, H. Nehrir, X. Hu, Z. Hu, H. Aki, B. Zhao, Z. Miao, and K. Strunz, "A review of modeling, management, and applications of grid-connected li-ion battery storage systems," *IEEE Trans. Smart Grid*, vol. 13, no. 6, pp. 4505–4524, Nov. 2022.
- [3] Q. Zhang, F. Ju, S. Zhang, W. Deng, J. Wu, and C. Gao, "Power management for hybrid energy storage system of electric vehicles considering inaccurate terrain information," *IEEE Trans. Autom. Sci. Eng.*, vol. 14, no. 2, pp. 608–618, Apr. 2017.
- [4] E. Chemali, M. Preindl, P. Malysz, and A. Emadi, "Electrochemical and electrostatic energy storage and management systems for electric drive vehicles: State-of-the-Art review and future trends," *IEEE Journal of Emerging and Selected Topics in Power Electronics*, vol. 4, no. 3, pp. 1117–1134, Sep. 2016.
- [5] R. E. Araújo, R. de Castro, C. Pinto, P. Melo, and D. Freitas, "Combined sizing and energy management in EVs with batteries and supercapacitors," *IEEE Trans. Veh. Technol.*, vol. 63, no. 7, pp. 3062–3076, Sep. 2014.
- [6] Y. Liu, Z. Yang, X. Wu, D. Sha, F. Lin, and X. Fang, "An adaptive energy management strategy of stationary hybrid energy storage system," *IEEE Trans. Transp. Electrif.*, vol. 8, no. 2, pp. 2261–2272, Jun. 2022.
- [7] F. Díaz-González, C. Chillón-Antón, M. Llonch-Masachs, S. Galcerán-Arellano, J. Rull-Duran, J. Bergas-Jané, and E. Bullich-Massagué, "A hybrid energy storage solution based on supercapacitors and batteries for the grid integration of utility scale photovoltaic plants," *Journal of Energy Storage*, vol. 51, p. 104446, Jul. 2022.
- [8] D. Lemian and F. Bode, "Battery-Supercapacitor energy storage systems for electrical vehicles: A review," *Energies*, vol. 15, no. 15, p. 5683, Aug. 2022.
- [9] Y. Wang, L. Wang, M. Li, and Z. Chen, "A review of key issues for control and management in battery and ultra-capacitor hybrid energy storage systems," *eTransportation*, vol. 4, p. 100064, May 2020.
- [10] R. de Castro, H. Pereira, R. E. Araújo, J. V. Barreras, and H. C. Pangborn, "qTSL: A multilayer control framework for managing capacity, temperature, stress, and losses in hybrid balancing systems," *IEEE Trans. Control Syst. Technol.*, vol. 30, no. 3, pp. 1228–1243, May 2022.
- [11] J. Wang, B. Wang, L. Zhang, J. Wang, N. I. Shchurov, and B. V. Malozymov, "Review of bidirectional DC–DC converter topologies for hybrid energy storage system of new energy vehicles," *Green Energy and Intelligent Transportation*, vol. 1, no. 2, p. 100010, Sep. 2022.
- [12] Hui Li and F. Z. Peng, "Modeling of a new ZVS bi-directional dc-dc converter," *IEEE Trans. Aerosp. Electron. Syst.*, vol. 40, no. 1, pp. 272–283, Jan. 2004.
- [13] S. Shao, L. Chen, Z. Shan, F. Gao, H. Chen, D. Sha, and T. Dragicevic, "Modeling and advanced control of dual-active-bridge DC–DC converters: A review," *IEEE Trans. Power Electron.*, vol. 37, no. 2, pp. 1524–1547, Feb. 2022.
- [14] R. de Castro, C. Pinto, J. Varela Barreras, R. E. Araújo, and D. A. Howey, "Smart and hybrid balancing system: Design, modeling, and experimental demonstration," *IEEE Trans. Veh. Technol.*, vol. 68, no. 12, pp. 11449–11461, Dec. 2019.
- [15] P. He and A. Khaligh, "Comprehensive analyses and comparison of 1 kw isolated DC–DC converters for bidirectional EV charging systems," *IEEE Transactions on Transportation Electrification*, vol. 3, no. 1, pp. 147–156, Mar. 2017.
- [16] F. Gao and D. Rogers, "Duty-cycle plus phase-shift control for a dual active half bridge based bipolar DC microgrid," in *2018 IEEE Applied Power Electronics Conference and Exposition*, 2018.
- [17] F. Gao, N. Mugwisi, and D. J. Rogers, "Average modeling of a Dual-Half-Bridge converter modulated with three degrees of freedom," *IEEE Transactions on Transportation Electrification*, vol. 7, no. 3, pp. 1016–1030, Sep. 2021.
- [18] Hui Li, Fang Zheng Peng, and J. S. Lawler, "A natural ZVS medium-power bidirectional DC–DC converter with minimum number of devices," *IEEE Trans. Ind. Appl.*, vol. 39, no. 2, pp. 525–535, Mar. 2003.
- [19] S. Chakraborty and S. Chattopadhyay, "Minimum-RMS-Current operation of asymmetric dual active Half-Bridge converters with and without ZVS," *IEEE Trans. Power Electron.*, vol. 32, no. 7, pp. 5132–5145, Jul. 2017.
- [20] K. Xiangli, S. Li, and K. M. Smedley, "Decoupled PWM plus Phase-Shift control for a Dual-Half-Bridge bidirectional DC–DC converter," *IEEE Trans. Power Electron.*, vol. 33, no. 8, pp. 7203–7213, Aug. 2018.
- [21] F. Gao, N. Mugwisi, and D. Rogers, "Three degrees of freedom operation of a dual half bridge," in *21st European Conference on Power Electronics and Applications*, 2019.
- [22] A. Tong, L. Hang, H. S.-H. Chung, and G. Li, "Using Sampled-Data modeling method to derive equivalent circuit and linearized control method for Dual-Active-Bridge converter," *IEEE Journal of Emerging and Selected Topics in Power Electronics*, vol. 9, no. 2, pp. 1361–1374, Apr. 2021.
- [23] M. S. Irfan, A. Ahmed, J. Park, and C. Seo, "Current-Sensorless Power-Decoupling Phase-Shift Dual-Half-Bridge converter for DC–AC power conversion systems without electrolytic capacitor," *IEEE Trans. Power Electron.*, vol. 32, no. 5, pp. 3610–3622, May 2017.
- [24] Y. Wu, M. Mahmud, Y. Zhao, and H. Mantooth, "Uncertainty and disturbance estimator-based robust tracking control for dual-active-

$$\begin{aligned}
A_{sx}(u) &= \begin{bmatrix} -\frac{R_b}{L_b} & -\frac{d}{L_b} & -\frac{d}{L_b} & 0 & 0 \\ \frac{d}{C_1} & -\frac{\pi d^2(d-1)}{C_1 L_r \omega_s} & -\frac{\pi d(d-1)^2}{C_1 L_r \omega_s} & \frac{4\pi^2 d^3 + 4\pi d^2 \phi - 4\pi^2 d^2 - 4\pi d \phi + \phi^2}{4 C_1 L_r \omega_s \pi} & \frac{4\pi^2 d^3 + 4\pi d^2 \phi - 8\pi^2 d^2 - 4\pi d \phi + 4\pi^2 d + \phi^2}{4 C_1 L_r \omega_s \pi} \\ \frac{d}{C_2} & -\frac{\pi d^2(d-1)}{C_2 L_r \omega_s} & -\frac{\pi d(d-1)^2}{C_2 L_r \omega_s} & \frac{4\pi^2 d^3 + 4\pi d^2 \phi - 4\pi^2 d^2 - 4\pi d \phi + \phi^2}{4 C_2 L_r \omega_s \pi} & \frac{4\pi^2 d^3 + 4\pi d^2 \phi - 8\pi^2 d^2 - 4\pi d \phi + 4\pi^2 d + \phi^2}{4 C_2 L_r \omega_s \pi} \\ 0 & A_{sx,3,2} & A_{sx,3,3} & -\frac{L_r \omega_s - \pi R_{sc} d^2 + \pi R_{sc} d^3 + R_{sc} d^2 \phi}{C_{sc1} L_r R_{sc} \omega_s} & -\frac{d(d-1)(\phi - \pi + \pi d)}{C_{sc1} L_r \omega} \\ 0 & A_{sx,4,2} & A_{sx,4,3} & -\frac{d^2(\phi - \pi + \pi d)}{C_{sc2} L_r \omega_s} & A_{sx,4,5} \end{bmatrix} \\
A_{sm}(u) &= \begin{bmatrix} 0 & 0 \\ -\frac{d}{C_1} & 0 \\ \frac{d-1}{C_1} & 0 \\ 0 & -\frac{d}{C_{sc1}} \\ 0 & -\frac{d-1}{C_{sc2}} \end{bmatrix} \tag{62}
\end{aligned}$$

$$B_s(u) = \begin{bmatrix} \frac{1}{L_b} \\ 0 \\ 0 \\ 0 \\ 0 \end{bmatrix} \tag{63}$$

$$A_{mx}(u) = \begin{bmatrix} 0 & \frac{d}{L_{m1}} & \frac{1-d}{L_{m1}} & 0 & 0 \\ 0 & 0 & 0 & \frac{d}{L_{m2}} & \frac{1-d}{L_{m2}} \end{bmatrix} \tag{64}$$

$$A_{sx,3,2} = -\frac{-4\pi^2 d^3 + 4\pi^2 d^2 - 4\pi d \phi + \phi^2}{4 C_{sc1} L_r \omega_s \pi}, \quad A_{sx,3,3} = \frac{4\pi^2 d^3 - 8\pi^2 d^2 + 4\pi^2 d - \phi^2}{4 C_{sc1} L_r \omega_s \pi} \tag{65}$$

$$A_{sx,4,2} = -\frac{-4\pi^2 d^3 + 4\pi^2 d^2 - 4\pi d \phi + \phi^2}{4 C_{sc2} L_r \omega_s \pi}, \quad A_{sx,4,3} = \frac{4\pi^2 d^3 - 8\pi^2 d^2 + 4\pi^2 d - \phi^2}{4 C_{sc2} L_r \omega_s \pi} \tag{66}$$

$$A_{sx,4,5} = -\frac{L_s \omega + \pi R_{sc} d - R_{sc} d \phi - 2\pi R_{sc} d^2 + \pi R_{sc} d^3 + R_{sc} d^2 \phi}{C_{sc2} L_s R_{sc} \omega} \tag{67}$$

Fig. 23. Definition of the auxiliary matrices employed in the DHB average model (10).

bridge converters,” *IEEE Trans. Transp. Electrif.*, vol. 6, pp. 1791–1800, Dec. 2020.

- [25] N. Tiwary, V. Naik N, A. K. Panda, A. Narendra, and R. K. Lenka, “A robust voltage control of DAB converter with super-twisting sliding mode approach,” *IEEE J. Emerg. Sel. Top. Ind. Electron.*, vol. 4, no. 1, pp. 288–298, Jan. 2023.
- [26] K. J. P. Veeramraju, A. Cardoza, J. Sarangapani, and J. W. Kimball, “Robust modifications to model reference adaptive control for reference voltage tracking in a dual active bridge dc-dc converter,” in *2022 IEEE Energy Conversion Congress and Exposition (ECCE)*. IEEE, Oct. 2022, pp. 1–7.
- [27] H. K. Khalil, *Nonlinear Systems*, ser. 3rd ed. Upper Saddle River, NJ: Prentice-Hall, 2002.
- [28] J. Ackermann, *Robust Control: The Parameter Space Approach*. Springer, 2002.
- [29] R. Errouissi, H. Shareef, A. Viswambharan, and A. Wahyudie, “Disturbance-observer-based feedback linearization control for stabilization and accurate voltage tracking of a DC-DC boost converter,” *IEEE Trans. Ind. Appl.*, vol. 58, no. 5, pp. 6687–6700, Sep. 2022.
- [30] V. Repecho, J. M. Olm, R. Grino, A. Doria-Cerezo, and E. Fossas, “Modelling and nonlinear control of a magnetically coupled multiport DC-DC converter for automotive applications,” *IEEE Access*, vol. 9, pp. 63 345–63 355, 2021.
- [31] T. A. Johansen and T. I. Fossen, “Control allocation—a survey,” *Automatica*, vol. 49, no. 5, pp. 1087–1103, May 2013.
- [32] R. de Castro and J. Brembeck, “Lyapunov-based control allocation for over-actuated nonlinear systems,” in *2019 American Control Conference (ACC)*, Jul. 2019, pp. 5033–5038.
- [33] S. Ijaz, M. Galea, M. T. Hamayun, H. Ijaz, and U. Javaid, “A new output integral sliding mode Fault-Tolerant control and fault estimation scheme for uncertain systems,” *IEEE Trans. Autom. Sci. Eng.*, vol. PP, no. 99, pp. 1–12.
- [34] X. Yu, P. Li, and Y. Zhang, “Fixed-Time actuator fault accommodation applied to hypersonic gliding vehicles,” *IEEE Trans. Autom. Sci. Eng.*,

vol. 18, no. 3, pp. 1429–1440, Jul. 2021.

- [35] F. Cao and X. He, “Online active fault detection for Over-Actuated systems with prescribed control performance,” *IEEE Trans. Autom. Sci. Eng.*, vol. 21, no. 1, pp. 4–14, Jan. 2024.
- [36] Z. Li, V. Bégoč, A. Chriette, and I. Fantoni, “Wrench capability analysis and control allocation of a collaborative Multi-Drone grasping robot,” *J. Mech. Robot.*, vol. 15, no. 2, p. 021003, Jun. 2022.
- [37] F. M. Ibanez, “Analyzing the need for a balancing system in supercapacitor energy storage systems,” *IEEE Trans. Power Electron.*, vol. 33, no. 3, pp. 2162–2171, Mar. 2018.
- [38] R. de Castro, J. Brembeck, and R. E. Araujo, “Nonlinear control of dual half bridge converters in hybrid energy storage systems,” in *2020 IEEE Vehicle Power and Propulsion Conference (VPPC)*. IEEE, Nov. 2020, pp. 1–5.
- [39] F. de Leon, A. Farazmand, and P. Joseph, “Comparing the T and π equivalent circuits for the calculation of transformer inrush currents,” *IEEE Trans. Power Delivery*, vol. 27, no. 4, pp. 2390–2398, Oct. 2012.
- [40] J. Sun and H. Grotstollen, “Averaged modelling of switching power converters: reformulation and theoretical basis,” in *23rd Annual IEEE Power Electronics Specialists Conference*, 1992.
- [41] M. Gopal, *Control Systems: Principles and Design*. McGraw-Hill, 2002.
- [42] John C. Doyle, Bruce A. Francis, Allen R. Tannenbaum, *Feedback Control Theory*. Macmillan Publishing Co., 1990.
- [43] R. Schlesinger and J. Biela, “Comparison of analytical models of transformer leakage inductance: Accuracy versus computational effort,” *IEEE Trans. Power Electron.*, vol. 36, no. 1, pp. 146–156, Jan. 2021.
- [44] W. Sienel, T. Bunte, and J. Ackermann, “PARADISE-Parametric robust analysis and design interactive software environment: a matlab-based robust control toolbox,” in *Proceedings of Joint Conference on Control Applications Intelligent Control and Computer Aided Control System Design*, Sep. 1996, pp. 380–385.



R. de Castro (Senior Member, IEEE) received his Licenciatura and Ph.D. degrees in Electrical and Computer Engineering from the University of Porto, Portugal, in 2006 and 2013, respectively. From 2007 to 2008, he was the co-founder of the startup We-MoveU, focusing on developing powertrain control solutions for lightweight electric vehicles. From 2013 to 2020, he was with the German Aerospace Center (DLR), Institute of System Dynamics and Control (SR), where he worked on enabling technologies for electric mobility and automated driving.

In 2021, he joined the University of California, Merced, as an Assistant Professor in the Department of Mechanical Engineering.

His current research focuses on controls and optimization for zero-emission and robotic vehicles. Ricardo holds four patents and has authored over 100 papers in international journals, conferences, and book chapters. He is a recipient of three best paper awards from IEEE and ASME, as well as the Hellman Fellowship Award, which recognizes outstanding early-career faculty within the University of California system. Ricardo serves as an Associate Editor for IEEE Transactions on Vehicular Technology and IEEE Access. He is also the Vice President for Motor Vehicles at the IEEE Vehicular Technology Society, the founding Chair of the IEEE Automated Vehicles Standards Committee (AVSC), and the General Chair of the 2022 IEEE Vehicle Power and Propulsion Conference (VPPC).



Rui Esteves Araujo (Member IEEE) received the Electrical Engineering diploma (5-year university degree) from University of Porto, Porto, Portugal, and the M.Sc. and Ph.D. degrees in Electrical and Computer Engineering from the University of Porto, Porto, Portugal, in 1992 and 2001, respectively. From 1987 to 1988, he was an Electrotechnical Engineer in Project Department of Adira - Metal Forming Solutions Company, Porto, Portugal, and from 1988 to 1989, he was Researcher with INESC, Porto, Portugal. Since 1989, he has been with the

University of Porto, where he is currently an Associate Professor with the Department of Electrical and Computer Engineering, Faculty of Engineering, University of Porto. He is Senior Researcher in the INESC TEC, focusing on power electronics systems and its industrial applications to motion control, electric vehicles and renewable energies.



Jonathan Brembeck received his Dipl.-Ing. (M.Sc.) degree in Mechanical Engineering (System Control and Electronics/Informatics) and his Dr.-Ing. (Ph.D.) in Electrical Engineering from Technical University of Munich, Munich, Germany, in 2008 and 2018, respectively. He started his career as a simulation engineer in the automotive industry. In 2009 he changed to the German Aerospace Center (DLR) as a researcher and project leader of ROboMObil, the robotic electric vehicle. His research interests include modeling of multi-physical systems and the nonlinear state estimation and control for autonomous vehicles. Since 2014 he has been the head of Department Vehicle System Dynamics and Control at DLR. In 2018 he started as a lecturer at the Technical University of Munich for the simulation of mechatronic systems. Dr. Brembeck Jonathan received the eCarTec Award 2012 (Bavarian national award for electro mobility) for the ROboMObil concept car and was awarded European Satellite Navigation Competition – Special Topic Winner 2011.